

# LSD: Lyman-break galaxies Stellar populations and Dynamics – I. Mass, metallicity and gas at $z \sim 3.1$ <sup>★</sup>

F. Mannucci,<sup>1,†</sup> G. Cresci,<sup>1,2</sup> R. Maiolino,<sup>3</sup> A. Marconi,<sup>4</sup> G. Pastorini,<sup>4</sup> L. Pozzetti,<sup>5</sup>  
A. Gnerucci,<sup>4</sup> G. Risaliti,<sup>1,6</sup> R. Schneider,<sup>1</sup> M. Lehnert<sup>7</sup> and M. Salvati<sup>1</sup>

<sup>1</sup>INAF - Osservatorio Astrofisico di Arcetri, Largo E. Fermi 5, I-50125 Firenze, Italy

<sup>2</sup>Max-Planck-Institut für extraterrestrische Physik (MPE), Giessenbachstr. 1, D-85748 Garching, Germany

<sup>3</sup>INAF - Osservatorio Astronomico di Roma, via di Frascati 33, I-00040 Monte Porzio Catone, Italy

<sup>4</sup>Dip. di Astronomia e Scienza dello Spazio, Università di Firenze, Largo E. Fermi 2, I-50125 Firenze, Italy

<sup>5</sup>INAF - Osservatorio Astronomico di Bologna - via Ranzani 1, I-40127 Bologna, Italy

<sup>6</sup>Harvard-Smithsonian Center for Astrophysics, 60 Garden Street, Cambridge, MA 02138, USA

<sup>7</sup>GEPI, Observatoire de Paris, CNRS, University Paris Diderot, 5 Place Jules Janssen, F-92190 Meudon, France

Accepted 2009 June 2. Received 2009 June 1; in original form 2009 February 13

## ABSTRACT

We present the first results of a project, Lyman-break galaxies Stellar populations and Dynamics (LSD), aimed at obtaining spatially resolved, near-infrared (IR) spectroscopy of a complete sample of Lyman-break galaxies at  $z \sim 3$ . Deep observations with adaptive optics resulted in the detection of the main optical lines, such as [O II]  $\lambda 3727$ , H $\beta$  and [O III]  $\lambda 5007$ , which are used to study sizes, star formation rates (SFRs), morphologies, gas-phase metallicities, gas fractions and effective yields. Optical, near-IR and *Spitzer*/Infrared Array Camera photometry are used to measure stellar mass. We obtain that morphologies are usually complex, with the presence of several peaks of emissions and companions that are not detected in broad-band images. Typical metallicities are 10–50 per cent solar, with a strong evolution of the mass–metallicity relation from lower redshifts. Stellar masses, gas fraction and evolutionary stages vary significantly among the galaxies, with less massive galaxies showing larger fractions of gas. In contrast with observations in the local universe, effective yields decrease with stellar mass and reach solar values at the low-mass end of the sample. This effect can be reproduced by gas infall with rates of the order of the SFRs. Outflows are present but are not needed to explain the mass–metallicity relation. We conclude that a large fraction of these galaxies is actively creating stars after major episodes of gas infall or merging.

**Key words:** galaxies: abundances – galaxies: formation – galaxies: high-redshift – galaxies: starburst.

## 1 INTRODUCTION

Metallicity is one the most important properties of galaxies, and its study is able to shed light on the details of galaxy formation. It is an integrated property, not related to the present level of star formation (SF), but rather to the whole past history of the galaxy. In particular, metallicity is sensitive to the fraction of baryonic mass already converted into stars, i.e. to the evolutionary stage of the galaxy.

Furthermore, metallicity is affected by the presence of infalls and outflows, i.e. by feedback processes and by the interplay between the forming galaxy and the intergalactic medium (IGM).

The existence of a clear correlation between luminosity and metallicity of galaxies is known from the late 1970s (Lequeux et al. 1979). It is now clear that local galaxies follow a well-defined mass–metallicity relation, where galaxies with larger stellar mass or larger circular velocity have higher metallicities (Garnett 2002; Pérez-González et al. 2003; Pilyugin, Vílchez & Contini 2004; Tremonti et al. 2004; Lee et al. 2006; Hayashi et al. 2008; Kewley & Ellison 2008; Liu et al. 2008; Michel-Dansac et al. 2008; Panter et al. 2008). The origin of the relation is uncertain because several effects can be, and probably are, active. It is well known that, in the local universe, starburst galaxies eject a significant amount of metal-enriched gas into the IGM because of energetic feedback from exploding supernovae (SNe; see, for example, Lehnert & Heckman

<sup>★</sup>Based on observations collected with European Southern Observatory/Very Large Telescope (ESO/VLT) (proposals 075.A-0300 and 076.A-0711), with the Italian TNG, operated by FGG (INAF) at the Spanish Observatorio del Roque de los Muchachos, and with the *Spitzer Space Telescope*, operated by JPL (Caltech) under a contract with NASA.

†E-mail: filippo@arcetri.astro.it

1996a; Mori, Umemura & Ferrara 2004; Scannapieco et al. 2008, and references therein). Numerous studies have shown that outflows are already present at high redshifts (Pettini et al. 2001, 2002; Frye, Broadhurst & Benítez 2002; Weiner et al. 2008). Outflows are expected to be more important in low-mass galaxies, where the gravitational potential is lower and a smaller fraction of gas is retained. As a consequence, higher mass galaxies are expected to be more metal rich (see, for example, Edmunds 1990; Garnett 2002).

A second possible effect shaping the mass–metallicity relation is related to the well-known effect of ‘downsizing’ (e.g. Cowie et al. 1996; Gavazzi & Scodeggio 1996), i.e. lower mass galaxies form their stars later and on longer time-scales than more massive systems. At a given time, lower mass galaxies have formed a smaller fraction of their stars, therefore, are expected to show lower metallicities (Ellison et al. 2008). Recently, Calura et al. (2009) have explained the evolution of the mass–metallicity relation up to  $z = 3.5$  as due to an increase of the efficiency of SF with galaxy mass, without invoking differential galactic outflows.

Other possibilities exist, for example some properties of SF, as the initial mass function (IMF), could change systematically with galaxy mass (Köppen, Weidner & Kroupa 2007).

All these effects have a deep impact on galaxy evolution, and the knowledge of their relative contributions is of crucial importance. Different models have been built to reproduce the shape of the mass–metallicity relation in the local universe, and different assumptions produce divergent predictions at high redshifts ( $z > 2$ ). It is possible to test these predictions as metallicities can now be measured at high redshifts (Kobulnicky & Koo 2000; Pettini et al. 2001, 2002; Maier et al. 2006). To explore this issue several groups have observed the mass–metallicity relation in the distant universe, around  $z = 0.7$  (Savaglio et al. 2005; Rodrigues et al. 2008), between 0 and 1.5 (Cowie & Barger 2008), between 0.5 and 1.2 (Lamareille et al. 2008; Perez-Montero et al. 2008) and at  $z \sim 2$  (Erb et al. 2006a; Halliday et al. 2008; Hayashi et al. 2008). They have found a clear evolution with cosmic time, with metallicity decreasing with increasing redshift, for a given stellar mass. Erb et al. (2006a,c) used near-infrared (IR) long-slit spectra of a large number of Lyman-break galaxies (LBGs) at  $z \sim 2$  to estimate the average amount of extinction and estimate the intrinsic star formation rate (SFR). By assuming that the Schmidt law holds at  $z = 2$  (see below), they also derive the fraction of baryonic mass in gas, and measure the effective yields.

There are several reasons to explore even higher redshifts. The redshift range at  $z \sim 3$ –4 is particularly interesting: it is before the peak of the cosmic SF density (see, for example, Hopkins & Beacom 2006; Mannucci et al. 2007), only a small fraction ( $\sim 15$  per cent; Pozzetti et al. 2007) of the total stellar mass ( $M_*$ ) has already been created, it is the redshift range where the most massive early-type galaxies are expected to form (see, for example, Saracco et al. 2003), the number of mergers among the galaxies is much larger than at later times (Conselice et al. 2007; Stewart et al. 2008). As a consequence, it is above  $z \sim 3$  that predictions of different models tend to diverge significantly, and it is important to sample this redshift range observationally. The observations are really challenging because of the faintness of the targets and the precision required to obtain a reliable metallicity. Nevertheless, the new integral-field unit (IFU) instruments on 8-m class telescopes are sensitive enough to allow for the project.

Metallicity at  $z \sim 3$  can be obtained by measuring the fluxes of the main optical emission lines ([O II]  $\lambda 3727$ , H $\beta$ , [O III]  $\lambda 5007$ , H $\alpha$ ), whose ratios have been calibrated against metallicity in the local universe (Nagao, Maiolino & Marconi 2006; Kewley &

Ellison 2008 and references therein). Of course, this method can be applied only to line-emitting galaxies, i.e. to low-extinction, star-forming galaxies, whose lines can be observed even at high redshifts (e.g. Teplitz et al. 2000; Pettini et al. 2001, 2002; Erb et al. 2006a). In contrast, the gas metallicity of more quiescent and/or dust-extincted galaxies, like extremely red galaxies (EROs; Mannucci et al. 2002), distant red galaxies (DRGs; Franx et al. 2003) and submm galaxies (SMGs; Chapman et al. 2005), cannot be easily measured at high redshifts. Stellar metallicities, revealed by absorption lines, can also be measured (Gallazzi et al. 2006; Halliday et al. 2008; Panter et al. 2008), but at  $z > 3$  this is even more observationally challenging.

Together with metallicity, the dynamical properties of galaxies have a special role for their understanding. Dynamics is directly related to the models of galaxy formation and it is the most direct way to probe the content of dark matter.

Not much is known about dynamics of high-redshift galaxies as high-resolution, high-sensitivity, spectroscopic observations are required. Nesvadba et al. (2006) and Stark et al. (2008) observed highly lensed LBGs at  $z \sim 3.1$  to obtain the velocity field. In these cases, the high spatial resolution on the source plane is provided by the presence of the gravitational lens, distorting the galaxy and stretching its apparent dimensions to several arcsec. Nesvadba et al. (2006) found rotation velocities of  $75 \text{ km s}^{-1}$  within the central lens-corrected 0.5 kpc, revealing the presence of a dynamical mass  $\log(M/M_\odot) = 9.3$ . Stark et al. (2008) found a well-ordered source, similar to local spirals. Förster Schreiber et al. (2006) obtained seeing-limited near-IR integral field spectroscopy of a large sample of galaxies at  $z \sim 2$ . A significant fraction of this composite sample of spatially extended, H $\alpha$ -emitting galaxies shows dynamical properties consistent with being the precursor of normal disc galaxies in the local universe. Other recent works by Bouché et al. (2007), Genzel et al. (2008) and Cresci et al. (2009) are addressing this problem, and the amount of accumulated information is rapidly growing.

Aimed at studying the high-redshift metallicity and dynamics, we started two projects, AMAZE (Assessing the Mass-Abundance redshift Evolution) and LSD (Lyman-break galaxies Stellar populations and Dynamics).<sup>1</sup> For both projects we observed a sample of galaxies at  $z = 3$ –4 with an IFU three-dimensional (3D) spectrograph in order to derive their chemical and dynamical properties. 3D spectroscopy is a key technique for these studies as it allows to derive the full velocity field of the galaxies, without the need to restrict the study to a slit. Furthermore, integrated spectra of the galaxies can be obtained without slit losses. This is particularly important when the flux ratios between lines at different wavelengths are derived, as differential losses can spoil the results.

For AMAZE, described in Maiolino et al. (2008), we selected 30 galaxies with deep *Spitzer*/Infrared Array Camera (IRAC) photometry (3.6–8  $\mu\text{m}$ ), an important piece of information to derive a reliable stellar mass. These galaxies were observed, in seeing-limited mode, with the IFU spectrometer SINFONI on European Southern Observatory/Very Large Telescope (ESO/VLT).

The aim of LSD is not only to measure metallicities, but also to obtain spatially resolved spectra to measure dynamics and spectral gradients. For this reason we used adaptive optics to improve the spatial resolution. Furthermore, we selected a complete, albeit

<sup>1</sup> This acronym is not to be confused with two others often used by astronomers, one of which is ‘Lens Structure and Dynamics’ by Koopmans & Treu (2003).

**Table 1.** Target list and summary of the observations.

(1) Object	(2) RA (J2000)	(3) Dec.	(4) $R_{AB}$	(5) $z_{em}$	(6) Dist (arcsec)	(7) SINFONI $R$ mag	(8) Scale	(9) $T_{exp}$	(10) $T(1+3)$	(11) <i>Spitzer</i> $T(2+4)$	(12) N/A
SSA 22a–C30	22:17:19.3	+00:15:44.7	24.2	3.103	35	13.0	$50 \times 100$	240	50	50	A
SSA 22a–C6	22:17:40.9	+00:11:26.0	23.4	3.097	35	12.0	$125 \times 250$	280	83	133	N
SSA 22a–M4	22:17:40.9	+00:11:27.9	24.8	3.098	35	12.0	$125 \times 250$	280	83	133	N
SSA 22b–C5	22:17:47.1	+00:04:25.7	25.2	3.112	11	14.9	$50 \times 100$	240	83	133	N
DSF 2237b–D28	22:39:20.2	+11 55 11.3	24.5	2.933	26	13.1	$50 \times 100$	240	96	96	A
DSF 2237b–MD19	22:39:21.1	+11 48 27.7	24.5	2.611	20	14.1	$50 \times 100$	200	–	–	–
Q0302–C131	03:04:35.0	–00:11:18.3	24.5	3.235	26	13.4	$50 \times 100$	240	332	133	N
Q0302–M80	03:04:45.7	–00:13:40.6	24.1	3.414	15	14.5	$50 \times 100$	240	166	399	N
Q0302–C171	03:04:44.3	–00:08:23.2	24.6	3.328	33	14.6	$50 \times 100$	240	332	–	N
Q0302–MD287	03:04:52.8	–00:09:54.6	24.8	2.395	13	15.0	$50 \times 100$	160	249	–	N

Columns: (1)–(3): target name and coordinates; (4): target  $R$ -band magnitude; (5): redshift from emission lines; (6)–(7): guide star distance and  $R$ -band magnitude; (8)–(9): spatial scale (mas) and total exposure time (min) of the SINFONI observations; (10)–(11): exposure time (min) for *Spitzer*/IRAC observations in channels 1+3 and 2+4; (12) new (N) or archive (A) *Spitzer*/IRAC data.

small, sample of LBGs, in order to obtain results that can be applied to the LBG population as a whole. This is the first paper about LSD, focusing on the chemical properties, while the dynamical properties will be examined in a forthcoming paper.

In the following, we adopt a  $\Lambda$  cold dark matter ( $\Lambda$ CDM) cosmology with  $H_0 = 70 \text{ km s}^{-1}$ ,  $\Omega_m = 0.3$  and  $\Omega_\Lambda = 0.7$ . At  $z = 3.1$ , the universe is 2-Gyr old, 15 per cent of its current age.

## 2 SAMPLE SELECTION

Our sample of LBGs was extracted from the Steidel et al. (2003) catalogue, which contains about 1000 spectroscopically confirmed LBGs, selected in 17 fields down to a limiting magnitude of  $R_{AB} = 25.5$ . The parent catalogue was searched for the presence of bright stars ( $R < 15$ ) within  $\sim 35$  arcsec of each source, resulting in the selection of  $\sim 100$  sources. The presence of a bright foreground star is needed to drive the adaptive optics module and obtain a resolution comparable with the diffraction limit of an 8-m class telescope, about 0.1 arcsec in the near-IR. The best combinations of star brightness and distance from the target were selected to obtain the final sample of 10 objects presented in Table 1.

We emphasize that no other property was used to select the targets, thus the present sample, albeit small, should be representative of the LBG population in the Steidel et al. (2003) sample. This is shown in Fig. 1, which compares the distributions of  $R$ -band magnitude and  $(G - R)$  colour of the selected targets with those of the parent population of LBGs. The distributions of both quantities are similar, with no apparent biases.

In order to check the possible presence of active galactic nuclei (AGN), we inspected the available X-ray observations of these galaxies. For two objects, DSF 2237b–D28 and DSF 2237b–MD19, no X-ray observation is available. The other sources lay in the field of a deep *Chandra* observation (SSA 22) and in that of a quasar observed with *XMM–Newton*. No source is detected in the 0.5–10 keV range. In all cases, the off-centre position of the sources, and/or the short exposure time imply a relatively high upper limit for the X-ray flux, which, given the high redshift of the sources, corresponds to X-ray luminosities larger than  $\sim 10^{43} \text{ erg s}^{-1}$ . Although these limits cannot rule out the presence of an AGN, there is no direct evidence for it. In all cases we can exclude a dominant, quasar-like AGN contribution.

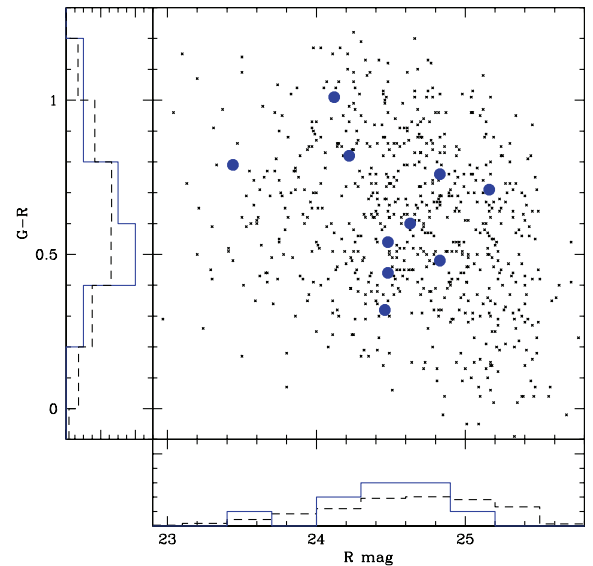


**Figure 1.** Distribution in  $R$  magnitude and  $(G - R)$  colour of the LSD targets (solid blue dots) compared to the spectroscopically confirmed targets of the Steidel et al. (2003) sample with  $2.5 < z < 3.3$  (small dots). The solid blue histograms show the distributions of these quantities for the LSD sample, which are similar to those for the total parent sample (dashed histograms).

## 3 OBSERVATIONS AND DATA REDUCTION

The selected objects have been observed with several instruments in order to obtain a complete data set.

### 3.1 Integral field spectroscopy

The targets were observed at ESO/VLT by using the SINFONI instrument (Eisenhauer et al. 2003; Bonnet et al. 2004), an IFU spectrograph fed by an adaptive optics module with a natural guide star (NGS). The IFU splits the incoming light into several adjacent slits, and a spectrum is obtained for each location in the field-of-view. Several spatial scales are available, corresponding to different spatial resolutions. For eight of the 10 targets we used the  $50 \times 100 \text{ mas pixel}^{-1}$  scale, providing a field-of-view of  $3 \times 3 \text{ arcsec}^2$ .

Such a scale is a good match of the theoretical diffraction limit in the  $K$  band on the VLT telescope, which is  $\sim 70$  mas, and the field-of-view is appropriate to observe galaxies of dimensions of  $\sim 1$  arcsec. Two objects constitute a pair of interacting galaxies at a distance of about 2 arcsec, in this case we used a larger scale,  $125 \times 250 \text{ mas pixel}^{-1}$  with a total field-of-view of  $8 \times 8 \text{ arcsec}^2$ .

In all cases we used the  $H + K$  grating, providing a simultaneous coverage of these two near-IR bands ( $1.5\text{--}2.4 \mu\text{m}$ ), with resolution  $\lambda/\Delta\lambda \sim 1400$  in the  $H$  band and  $\sim 1800$  in the  $K$  band.

Observations were divided into independent sequences of about 45 min each, due to the limitation of the ESO service observing strategy based on observing blocks (OBs) of about 1 h of total time. During each OB, an ABBA nodding was used, putting the target in two positions of the field-of-view about 1.5 arcsec apart. This is a very efficient way to observe compact objects as no time is lost in observing the sky. Nevertheless, in principle this could introduce some self-subtraction of the wings of the targets more extended than 1.5 arcsec.

A maximum seeing of 0.8 arcsec was requested to carry out the observations, and an image of the reference star was observed at the beginning of each OB to monitor the conditions of the atmosphere during the observations.

Data were reduced by using the ESO pipeline (Modigliani et al. 2007) with the improved sky subtraction described by Davies (2007). After flat-fielding, sky subtraction, correction for distortions and wavelength calibration, the two-dimensional (2D) data of each OB are mapped into a 3D data cube with dimensions  $32 \times 64 \times 2048$  pixels. The cubes of the different OBs are then combined together by measuring the relative offsets from the detected centroid of emission. We note that using the coordinates in the image header often does not provide the requested precision ( $< 0.1$  arcsec), as the measured pointing uncertainties are of the order of 0.2 arcsec.

### 3.2 Photometric and morphological data

The original data set of optical photometry in the  $UGR$  bands by Steidel et al. (2003) is available for all the objects. Such a limited wavelength range does not allow to obtain reliable stellar masses by fitting the spectral energy distribution (SED). The optical data must be complemented by near-IR photometry.  $J$ - and  $K$ -band photometry of four objects was published by Shapley et al. (2001). We have observed the remaining six objects in the  $J$  and  $K_s$  filters with the Near-Infrared Camera Spectrometer (NICS; Baffa et al. 2001) on the Italian 3.6-m telescope TNG. Exposure times of 1–1.5 h in  $J$  and 2–3.5 h in  $K_s$  were used, according to the expected near-IR magnitudes. NICS data were reduced by the automatic pipeline SNAP.<sup>2</sup>

Photometry at longer wavelengths ( $3.6\text{--}8 \mu\text{m}$ ) is available in the *Spitzer*/IRAC archive (Fazio et al. 2004; Werner et al. 2004) for some of the objects in the SSA 22 field. For the remaining objects we obtained targeted observation with *Spitzer*/IRAC during cycle 7, as listed in Table 1. We used the post-BSD products of the pipeline, and measured aperture photometry.

Finally, *Hubble Space Telescope* (*HST*) will observe these objects after SM4, both in the optical with Advanced Camera for Surveys (ACS) and in the near-IR with Wide Field Camera 3 (WFC3), providing accurate photometry and broad-band morphologies. In conclusion, these objects will have a complete set of photometric

and spectroscopic observations with detailed morphological information at optical and near-IR bands, and will be suitable for detailed studies.

## 4 RESULTS AND MEASURED QUANTITIES

### 4.1 The detected lines

The final SINFONI data cubes were searched for the position of the brightest lines, either [O III]  $\lambda 5007$  or  $H\alpha$ , to define the spatial position of the target. The main optical lines ([O II]  $\lambda 3727$ ,  $H\beta$ , [O III]  $\lambda 5007$  and  $H\alpha$ ) are detected in nine out of 10 galaxies, the only exception being Q0302–MD287. The reasons for this non-detection are not clear. It is possible that its emission lines fall below our detection threshold, or that they coincide with bright sky lines. The SED fitting described in Section 4.3 points toward the existence of a large amount of dust in this object, with  $A_V$  between 0.9 and 1.1 mag. As a consequence, it is also possible that the optical lines are not detected because of the presence of large amount of dust extinction.

The choice of the aperture for the extraction of the spectra is an important step. Measuring metallicity requires a good knowledge of line ratios, which are best obtained inside small apertures on the central regions of the galaxies, where the signal-to-noise ratio is higher. In contrast, measuring total SFRs requires larger apertures to maximize the fraction of line emission recovered by aperture photometry. To measure all these quantities, we extracted complete spectra inside a circular aperture of 0.35 arcsec of diameter, corresponding to 7 pixels, and an aperture correction for a point source was applied to recover the emitted flux of the central part of the galaxies. We chose a circular aperture, instead of more complex apertures based on object morphology and surface brightness, in order to avoid any problem with possible variations of the point spread function (PSF) with wavelength and a non-perfect spatial alignment of the spectra. The fraction of total flux recovered by this procedure was estimated by computing the curve of growth of the photometry of the brightest line as a function of aperture radius. A correction for the missing flux is applied when the ‘total’ quantities are needed. The results are shown in Table 2, listing the line fluxes inside the circular aperture and the correcting factor to total fluxes. Except for one galaxy, SSA 22a–C30, composed by several clumps of emission, for all the other galaxies the tabulated fluxes comprise more than half of the total flux.

### 4.2 Morphologies and sizes

Fig. 2 shows the images of all the targets. Most of the galaxies show a sharp peak of line emission and some extended structure. In several cases, the objects appear to be composed by several clumps of emission. The distance between clumps is usually comparable to the dimension of the objects as revealed by ground-based imaging. In a few cases the distribution of the secondary peaks follow the continuum light, while in some cases we detected faint ‘companions’ that are not detected in broad-band. VLT has a small pointing error, of the order of 0.2 arcsec, but, compared to our resolution, this is enough to introduce a significant uncertainty in the relative astrometry between ultraviolet (UV) and line images. As a consequence, we cannot be sure where the line emission originates with respect to the UV image. Assuming that the main peak of line emission corresponds to the maximum of the UV light, the line-emission ‘companions’ could be both secondary peak of SF and line emission inside a single formed galaxy, or the signature of an ongoing

<sup>2</sup> <http://www.arcetri.astro.it/~filippo/snap>

**Table 2.** Properties of the detected lines.

(1) Object	(2) Line	(3) $z$	(4) Flux <sup>a</sup>	(5) Fact <sup>b</sup>
SSA 22a–C30	[O II] 3727	3.1024	$0.30 \pm 0.12$	3.18
	H $\beta$	3.1030	$0.26 \pm 0.10$	
	[O III] 4958	3.1034	$0.34 \pm 0.10$	
	[O III] 5007	3.1026	$1.28 \pm 0.22$	
SSA 22a–C6	[O II] 3727	3.0966	$1.21 \pm 0.38$	1.09
	H $\beta$	3.0970	$0.76 \pm 0.45$	
	[O III] 4958	3.0966	$2.26 \pm 0.78$	
	[O III] 5007	3.0968	$5.50 \pm 0.62$	
SSA 22a–M4	[O II] 3727	3.0961	$1.46 \pm 0.23$	1.06
	H $\beta$	3.0976	$0.69 \pm 0.25$	
	[O III] 4958	3.0965	$1.08 \pm 0.30$	
	[O III] 5007	3.0978	$3.66 \pm 0.49$	
SSA 22b–C5	[Ne III] 3869	3.1098	$0.38 \pm 0.14$	1.57
	H $\beta$	3.1122	$0.50 \pm 0.14$	
	[O III] 4958	3.1120	$1.01 \pm 0.22$	
	[O III] 5007	3.1121	$3.28 \pm 0.24$	
D2237b–D28	[O II] 3727	2.9352	$0.74 \pm 0.16$	1.84
	[O III] 4958	2.9328	$0.50 \pm 0.16$	
	[O III] 5007	2.9324	$1.86 \pm 0.36$	
D2237b–MD19	H $\beta$	2.6093	$0.60 \pm 0.16$	1.95
	H $\alpha$	2.6108	$2.96 \pm 0.46$	
Q0302–C131	[O II] 3727	3.2349	$0.80 \pm 0.32$	1.29
	H $\beta$	3.2346	$0.46 \pm 0.16$	
	[O III] 4958	3.2341	$0.90 \pm 0.20$	
	[O III] 5007	3.2346	$2.62 \pm 0.52$	
Q0302–M80	[O II] 3727	3.4136	$0.56 \pm 0.18$	1.23
	H $\beta$	3.4138	$0.40 \pm 0.12$	
	[O III] 4958	3.3990	$0.42 \pm 0.20$	
	[O III] 5007	3.4137	$1.32 \pm 0.26$	
Q0302–C171	[O II] $\lambda$ 3727	3.3287	$0.56 \pm 0.24$	1.92
	H $\beta$	3.3289	$0.18 \pm 0.08$	
	[O III] $\lambda$ 4958	3.3280	$0.28 \pm 0.08$	
	[O III] $\lambda$ 5007	3.3279	$1.10 \pm 0.12$	

<sup>a</sup>Line flux inside an aperture of 0.35 arcsec with correction for the PSF, units of  $10^{-17}$  erg cm $^{-2}$  s $^{-1}$ .

<sup>b</sup>Scaling factor to total flux.

merging. A detailed comparison with broad-band, rest-frame UV morphology will be given on the basis of future *HST* images.

Images obtained with a NGS usually have a non-circular PSF (see, for example, Cresci et al. 2005). Increasing the distance of the scientific target from the NGS, the PSF becomes larger. The variation in the radial direction, i.e. towards the NGS, is larger than in the tangential direction. As a result, when this effect is dominant, the objects appear to be elongated toward the NGS. The magnitude of the effect depends on the conditions of the atmosphere and on the distance of the target from the NGS, and is of the order of 0.1–0.3 arcsec. In our images, elongation toward the NGS is seen only in one case, meaning that in most cases the atmospheric conditions were good enough for AO observations and the isoplanatic angle in the *K* band was not significantly smaller than the separation between the target and the guide star.

No bright point sources are present in our field-of-view, preventing us from measuring the final PSF on the combined data themselves. To estimate the PSF we used the on-axis image of the NGS taken every hour at the beginning of each OB. The on-axis

PSF full width at half-maximum (FWHM) was degraded to take into account the distance of the target galaxy from the NGS. For this we used the recipes in Cresci et al. (2005), using the values of the isoplanatic angle provided by the ESO data base, and averaging over the different values obtained for the different OBs. As the seeing was always comprised in the narrow range 0.6–1.0 arcsec FWHM, no large differences are seen in most of the OBs. In all cases we obtained values of the PSF FWHM of the order of 0.2 arcsec for the fields observed with the smallest spatial scale, and 0.3 arcsec for the fields with the largest scale. These values are in good agreement with the results of the simulations provided by ESO, and were used in the following analysis.

Galaxy sizes have been estimated by fitting a Moffat function to the image in the brightest line, and the results have been deconvolved for the PSF. The measured half-light radii are listed in Table 3. Large uncertainties on the resulting sizes are present, both because images usually have low signal-to-noise ratio (S/N) and because the PSF is not accurately known. Furthermore, companions and secondary peaks of emission are not considered in measuring the dimensions. As this is also true for line fluxes, the derived metallicities (Section 4.6) and gas mass (Section 6.3), are consistently derived from the main peak only.

Since we are observing faint galaxies with high spatial resolution, surface brightness is probably our limiting factor. The dimensions of the detected line-emitting regions are sometimes significantly smaller than the dimensions obtained in the UV by ground-based imaging, even taking into account the larger PSF. They are also smaller than object sizes obtained with SINFONI/VLT without the use of AO by the Spectroscopic Imaging survey in the Near-infrared with SINFONI (SINS; Förster Schreiber et al. 2006, although at  $z \sim 2.2$ ) and AMAZE (Maiolino et al. 2008) collaborations. We interpret these results as evidence that our detected sizes are indeed limited by surface brightness. The average limiting surface brightness is  $1.2 \times 10^{-16}$  erg cm $^{-2}$  s $^{-1}$  arcsec $^{-2}$ . Such a sensitivity can be translated into a limiting SFR density at  $z \sim 3.1$  detected with an emission line. For H $\beta$ , the limiting SFR density is  $\sim 4/M_{\odot}$  yr $^{-1}$  kpc $^{-2}$ ; for [O III]  $\lambda$ 5007, assuming an average ratio of [O III]  $\lambda$ 5007/H $\beta$  = 4, the minimum detectable SFR density is  $\sim 1 M_{\odot}$  yr $^{-1}$  kpc $^{-2}$ . This is similar to the SFR density at  $z = 2.2$  in Erb et al. (2006b), and it is adequate to detect a significant fraction of the local starbursts (Kennicutt 1998). Nevertheless, the outer, low surface brightness parts of these galaxies are probably lost in the noise, and morphologies could appear more compact than they actually are.

The measured half-light radii range between 0.7 and 2.4 kpc, with a median value of 1.36 kpc. These radii are similar to those in the sample of local starbursts in Lehnert & Heckman (1996b), who measure a median value of 1.70 kpc. Considering that our observations are less sensitive to the outer parts of the galaxies than Lehnert & Heckman (1996a), we conclude that LBGs tend to be as extended as local starbursts.

### 4.3 The stellar mass

Stellar masses ( $M_*$ ) are derived by fitting the SED with HYPERZ-MASS (Pozzetti et al. 2007), a modified version of the photometric redshift code HYPERZ (Bolzonella, Miralles & Pelló 2000). These fits also provide estimates of age, current SFR and dust extinction of the dominant stellar population. The presence of good IRAC photometry allows the determination of reliable  $M_*$  as the SED is sampled up to the rest-frame *J* band. We have used the Bruzual & Charlot (2003) spectrophotometric models of galaxy evolution and

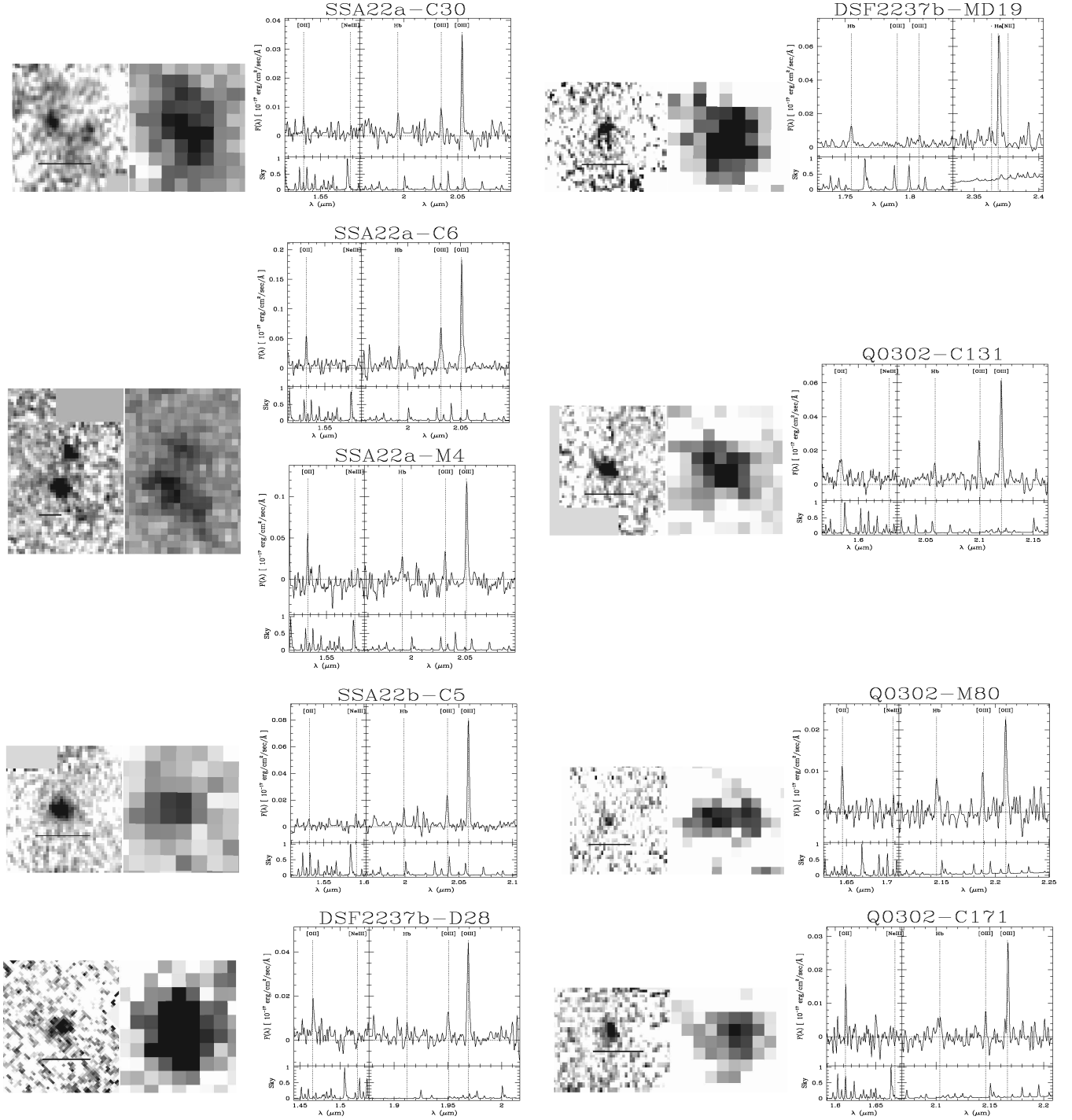


**Figure 2.** Images and spectra of the targets. For each object we show, from left to right: morphology in the emission line ( $H\alpha$  for MD 19,  $[O\text{III}] \lambda 5007$  for the others), ground-based  $R$ -band image by Steidel et al. (2003) and galaxy spectrum compared to the sky spectrum. The horizontal bars in the line images are 1-arcsec long. First column, from top to bottom: SSA 22a–C30, the interacting system composed by SSA 22a–C6 (south, upper spectrum) and SSA 22a–M4 (north, lower spectrum), SSA 22b–C5, DSF 2237b–D28. Second column: DSF 2237b–MD19, Q0302–C131, Q0302–M80 and Q0302–C171.

smooth exponentially decreasing SF histories, constraining the age to be smaller than the Hubble time at galaxy redshift, as detailed in Pozzetti et al. (2007).

The photometric stellar masses have typical dispersions due to statistical uncertainties and degeneracies of the order of 0.2 dex. Metallicity has little influence on the SED, with uncertainties of  $\sim 0.05$  dex, and we have set it to  $Z = 0.2 Z_{\odot}$ , in agreement with

what derived from the emission lines as described below. The addition of secondary bursts to a continuous SF history produces systematically higher (up to 40 per cent on average) stellar masses, while population synthesis models with TP-AGB phase (Maraston 2005) produce a systematic shift of  $\sim 0.1$  dex towards lower  $M_*$ . Finally, the uncertainty on the absolute value of the  $M_*$  due to the assumptions on the IMF is within a factor of 2 for the typical IMFs

**Table 3.** Properties of the target galaxies.

(1) Object	(2) $\log(M_*/M_\odot)$	(3) $A_{V,c}$ range	(4) $SFR_{em}$ ( $M_\odot \text{ yr}^{-1}$ )	(5) $r_{1/2}$ (kpc)	(6) $12 + \lg(O/H)$	(7) $\lg(M_{gas}/M_\odot)$	(8) $f_g$	(9) $\lg(Y_{eff})$
SSA 22a–C30	$10.33^{+0.31}_{-0.38}$	0.0–0.8	$29^{+81}_{-21}$	$1.48 \pm 0.44$	$8.16^{+0.20}_{-0.60}$	$9.66 \pm 0.41$	$0.18^{+0.26}_{-0.12}$	$-2.63^{+0.2+0.3}_{-0.7-0.2}$
SSA 22a–C6	$9.68^{+0.15}_{-0.06}$	0.3–0.5	$23^{+11}_{-8}$	$1.75 \pm 0.22$	$7.95^{+0.20}_{-0.50}$	$9.96 \pm 0.13$	$0.66^{+0.08}_{-0.12}$	$-2.22^{+0.2+0.1}_{-0.4-0.2}$
SSA 22a–M4	$9.41^{+0.34}_{-0.13}$	0.0–0.8	$20^{+40}_{-13}$	$2.01 \pm 0.27$	$8.12^{+0.25}_{-0.45}$	$9.96 \pm 0.34$	$0.78^{+0.12}_{-0.28}$	$-1.84^{+0.2+0.4}_{-0.4-0.4}$
SSA 22b–C5	$8.96^{+0.38}_{-0.22}$	0.0–0.5	$15^{+15}_{-8}$	$1.28 \pm 0.38$	$7.66^{+0.20}_{-0.20}$	$9.64 \pm 0.21$	$0.83^{+0.08}_{-0.19}$	$-2.17^{+0.2+0.3}_{-0.2-0.4}$
DSF 22–D28	$9.78^{+0.28}_{-0.29}$	0.0–0.6	$14^{+18}_{-8}$	$1.50 \pm 0.48$	$8.20^{+0.10}_{-0.25}$	$9.62 \pm 0.25$	$0.61^{+0.21}_{-0.20}$	$-2.32^{+0.1+0.3}_{-0.2-0.2}$
DSF 22–MD19	$10.06^{+0.33}_{-0.27}$	0.0–1.2	$39^{+77}_{-26}$	$2.00 \pm 0.55$	–	$9.98 \pm 0.33$	$0.69^{+0.25}_{-0.26}$	–
Q0302–C131	$10.09^{+0.10}_{-0.33}$	0.0–0.3	$10^{+6}_{-4}$	$1.27 \pm 0.37$	$8.00^{+0.25}_{-0.40}$	$9.57 \pm 0.14$	$0.42^{+0.13}_{-0.07}$	$-2.73^{+0.2+0.2}_{-0.4-0.1}$
Q0302–M80	$10.07^{+0.23}_{-0.19}$	0.0–0.6	$13^{+17}_{-8}$	$0.75 \pm 0.24$	$8.36^{+0.15}_{-0.15}$	$9.54 \pm 0.25$	$0.36^{+0.16}_{-0.12}$	$-2.37^{+0.1+0.2}_{-0.1-0.2}$
Q0302–C171	$10.06^{+0.10}_{-0.28}$	0.0–0.2	$5^{+2}_{-2}$	$1.25 \pm 0.39$	$8.14^{+0.25}_{-0.45}$	$9.26 \pm 0.11$	$0.30^{+0.08}_{-0.04}$	$-2.71^{+0.2+0.1}_{-0.4-0.1}$

Columns. (2)–(3): Stellar mass and dust extinction from SED fitting; (4): total SFR from emission lines; (5): half-light radius of line emission; (6): gas-phase metallicity (7)–(8): gas mass and gas fraction; (9): effective yields. The first error is due to metallicity, the second one to gas fraction.

usually adopted in the literature. We have used the Chabrier (2003) IMF with lower and upper cut-offs of 0.1 and  $100 M_\odot$ . The resulting stellar masses can be scaled to the standard Salpeter IMF by multiplying them by a factor of 1.7 (Pozzetti et al. 2007).

The results are shown in Table 3. The listed errors are due to both statistical uncertainties and degeneracies. Masses, expressed in  $\log(M_*/M_\odot)$ , range from 8.96 to 10.33, with a log average of 9.82. These values are consistent with those derived by Shapley et al. (2001) for their sample of LBGs at  $z \sim 3$ , averaging at 10.05 when converting their values to our IMF. Lower redshift BM/BX galaxies in the  $z \sim 2$  sample of Erb et al. (2006c) are also quite similar, with an average  $\log(M_*/M_\odot)$  of 10.22, within  $\sim 0.3$  of our average value.

Galaxy age, current SFR and dust extinction on the continuum  $A_{V,c}$  cannot be individually well constrained because they suffer of significant degeneracy. The errors associated to each of these three quantities are large, and this is particularly important for extinction which is used to estimate the total SFR from emission lines. The range of the allowed values of  $A_{V,c}$  is shown in Table 3. Despite the large errors, a possible correlation is seen between stellar mass and age, i.e. less massive galaxies are best fitted by younger templates. The best-fitting age is of the order of  $10^{7.5}$  yr for the less massive galaxies, and about  $10^9$  yr for the most massive ones.

#### 4.4 Photoionization conditions

The values of SFR and metallicity derived in the next sections are correct only if the optical line emission is dominated by SF and the conditions are not too different from those in the local universe. Even if the observed line ratios are typical of starburst galaxies, several problems could be present.

The first concern is that the presence of an AGN could alter line ratios and produce a spurious value of the inferred metallicity. No evidence of AGN is seen in the emission line shape, where the width of the forbidden lines is consistent with those of the permitted lines. This excludes the presence of a dominant broad-line AGN, but it does not help in excluding a narrow-line AGN (see the discussion in Section 2).

The second concern is that significant differences in the conditions of star-forming regions can be present, as LBGs at  $z \sim 3$  have larger SFRs than most galaxies in the local universe. In particular, any evolution of the photoionization conditions could mimic a

change of metallicity. The presence of evolution can be studied by comparing the flux ratios  $[N II]/H\alpha$  versus  $[O III]/H\beta$ , and several studies at lower redshift indicate that such an evolution actually exists (Shapley et al. 2005; Erb et al. 2006a; Brinchmann, Pettini & Charlot 2008; Liu et al. 2008). Line ratios discrepant from the local relation are often associated with higher SFR surface densities, interstellar pressures and ionization parameters.

We have verified that all the observed line ratios are fully consistent with excitation from hot stars, but we cannot study the presence of evolution because in most cases we cannot observe  $H\alpha$ . Nevertheless, several authors (Brinchmann et al. 2008; Liu et al. 2008) conclude that the influence of different ionization conditions on the derived metallicities is likely to be low, of the order of 0.1 dex.

#### 4.5 SFR from optical lines and SED fitting

SFR can be derived from the  $H\alpha$  and  $H\beta$  lines. Several conversions are possible, depending on the available data and physical condition of the galaxies. Similar to what is often done by many authors (e.g. Erb et al. 2006a; Förster Schreiber et al. 2009), we have used the ‘classical’ conversion factor by Kennicutt (1998), scaling down the results by a factor of 1.7 (Pozzetti et al. 2007) to convert them to the Chabrier (2003) IMF. The Kennicutt (1998) conversion factor is based on the  $H\beta$  flux corrected for dust extinction, and therefore requires a good knowledge of the amount of extinction  $A_{V,el}$  suffered by the emission lines. Calzetti et al. (2000) found that this is proportional to the extinction suffered by the continuum  $A_{V,c}$ , as measured by SED fitting, with  $A_{V,el} = A_{V,c}/0.44$  (see also Förster Schreiber et al. 2009), and here we have used this assumption. For DSF 2237b–D28 the  $H\beta$  flux is derived from  $[O III] \lambda 5007$  and the expected line ratio for the value of metallicity measured in the next section. The values of SFRs are listed in Table 3 and plotted in Fig. 3.

As explained in the previous section, large ranges of extinction are allowed by our SED fitting, therefore the resulting SFRs have large errors, with typical uncertainties of one order of magnitude. This is common to most of the studies of high-redshift star-forming galaxies, even if sometimes the errors on the SFR are not accurately discussed. Unfortunately, other possible conversion factors that could provide smaller uncertainties cannot be applied to high-redshift starburst galaxies. For example, several other estimates have been proposed by Moustakas, Kennicutt & Tremonti (2006),

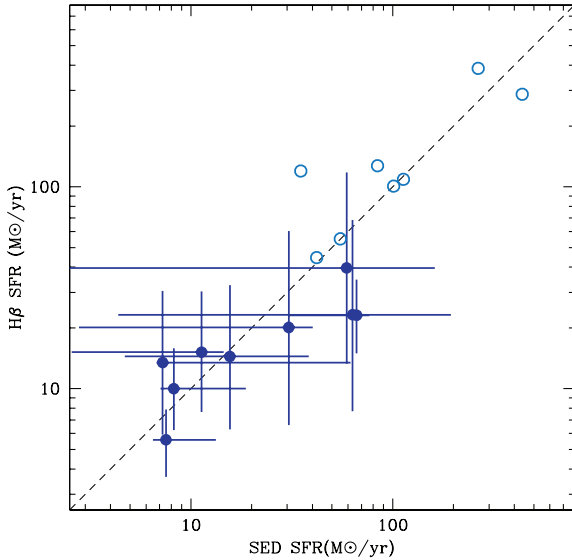


**Figure 3.** Comparison between the SFRs derived from SED fitting and line emission. Solid and empty dots show LSD and AMAZE galaxies, respectively. The dashed line shows equal SFRs. A good agreement is found between the two estimates of the SFR.

Weiner et al. (2007) and Argence & Lamareille (2008), based on a combination of two emission lines (such as [O II]  $\lambda 3727$  and H $\beta$ ), on lines and broad-band photometry, or line flux with no correction for dust extinction. These recipes are based on the empirical correlation among mass, SFR, dust extinction, luminosity and metallicity observed in local galaxies, and it is not possible to apply them for galaxies with very different properties.

The SFR derived from the emission lines can be compared with the value resulting from the fit of the SED (see Fig. 3). Large uncertainties are present due to the errors on H $\beta$  flux, the uncertainties in dust extinction correction for both estimates of SFR, the intrinsic spread of both calibrations. Nevertheless, a good agreement is seen between the two estimators of the SFR.

#### 4.6 Metallicity

Gas-phase metallicities were derived by comparing the observed line ratios with the calibrations in Nagao et al. (2006) and Maiolino et al. (2008). Metallicities are derived by a simultaneous fit of all the available line ratios, as explained in Maiolino et al. (2008). Both the uncertainties in the observed line ratios and the spread of the calibration were considered, and in some cases the latter is the dominant contribution to the metallicity error. In practice, the result is dominated by the R23 indicator or, similarly, by the [O III]  $\lambda 5007$ /H $\beta$  ratio, while the [O III]  $\lambda 5007$ /[O II]  $\lambda 3727$  ratio is used to discriminate between the two possible branches at low and high metallicity. The [Ne III] 3869/[O II] 3727 line ratio is also a sensitive indicator, when both lines are detected. The uncertainties on metallicity are of the order of 0.2–0.3 dex, and tend to be larger when the metallicity has values  $12 + \log(\text{O}/\text{H}) \sim 8$ , when both R23 and [O III]  $\lambda 4958$ , 5007/H $\beta$  have a maximum. In this case a small uncertainty in the line ratio produces a large uncertainty in metallicity. The results are listed in Table 3. LSD galaxies show metallicities about 10–50 per cent solar, similar to the values found by Pettini et al. (2001) for a different sample of LBGs at  $z \sim 3$ .

Dust extinction is not strongly affecting the results as the only extinction-sensitive line ratio is [O III]  $\lambda 5007$ /[O II]  $\lambda 3727$ . This ef-

fect can be clearly seen in fig. 6 of Maiolino et al. (2008), showing that metallicity is barely dependent on extinction and, as a consequence, the observed line ratios leave extinction basically unconstrained. For this reason we have chosen to limit the extinction to be within the range allowed by the SED fitting. Leaving extinction totally unconstrained does not affect the best-fitting value of metallicity but only the range of confidence.

## 5 NOTES ON INDIVIDUAL OBJECTS

### 5.1 SSA 22a–C30

This is the galaxy with the largest stellar mass. While H $\beta$  and [O III]  $\lambda 5007$  are in clean parts of the atmospheric spectrum, [O II]  $\lambda 3727$  and [O III]  $\lambda 4958$  are affected by OH lines. [O III]  $\lambda 5007$  emission is characterized by the presence of a secondary peak, about 1 arcsec apart from the main one. Other lower luminosity peaks can be present in between, although with lower significance. As a result, the object has a complex, very disturbed morphology. In the ground-based UV image, this galaxy appears less disturbed. It is elongated as the line-emitting blobs and can comprise them all.

### 5.2 SSA 22a–C6 and SSA 22a–M4

This is a pair of interacting galaxies at a projected distance of about 2 arcsec and with velocity difference of about  $300 \text{ km s}^{-1}$ . All lines, except [Ne III]  $\lambda 3869$ , fall far from the OH atmospheric lines, allowing for a good measurement of the metallicity. C6, the southernmost object, is the brightest member both in UV and in line emission. It has an elongated structure in the UV, and also the line image shows some secondary peaks coincident with the UV elongation. M4 is compact in both UV and line images.

### 5.3 SSA 22b–C5

This is the object with the smallest stellar mass, the only one with  $\log(M_*/M_\odot) < 9$ . While [O III]  $\lambda 4958$ , 5007 are well detected, [O II]  $\lambda 3727$  is hidden by a sky line. A marginally significant structure is detected near the expected position of the [Ne III]  $\lambda 3869$  line, providing a value of the redshift ( $z = 3.116$ ) slightly larger than the value from the [O III]  $\lambda 5007$  line ( $z = 3.112$ ). This could be a real detection of the [Ne III]  $\lambda 3869$  line, but both the low statistical significance and the small velocity offset make it quite uncertain. Here we assume that this is not a real line and do not use it to derive metallicity. The galaxy shape is regular and almost circular, with no significant structure around the main core.

### 5.4 DSF 22b–D28

The line image is characterized by a compact nucleus surrounded by an extended faint emission, with a size much more compact than in the broad-band image. Its emission lines are quite faint and H $\beta$  is not detected.

### 5.5 DSF 22b–MD19

This is the galaxy of our sample with the lowest redshift,  $z = 2.616$ , and it is the only one where H $\alpha$  can be observed. This line falls in the  $K$  band at  $2.37 \mu\text{m}$ , where the thermal contribution to the background is significant. Nevertheless, it is very well detected. The nearby [N II] lines are not detected and we can put a limit to their flux ratio with H $\alpha$  of  $[\text{N II}] 6583/\text{H}\alpha < 0.3$ . Such a value



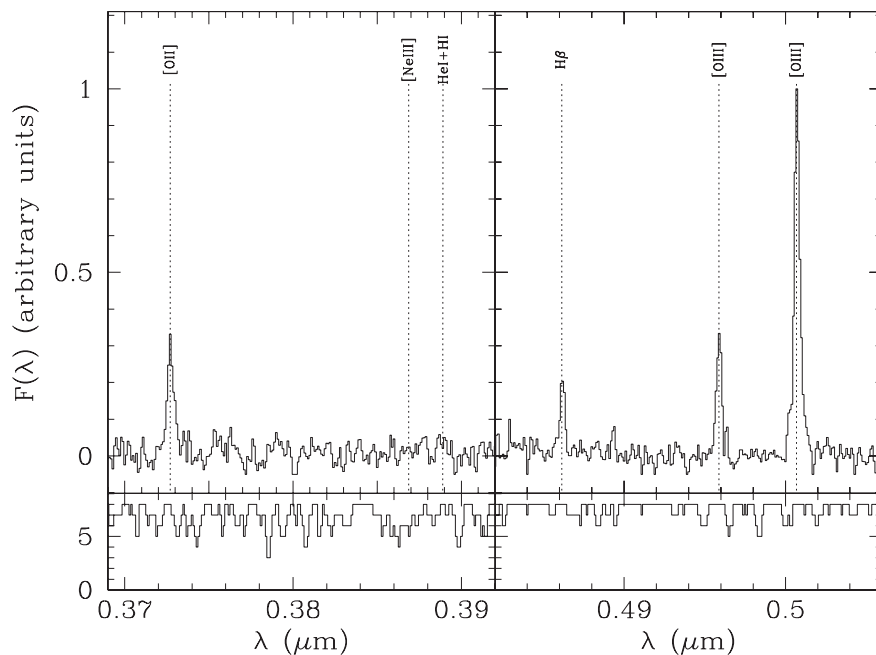


**Figure 4.** Composite spectrum obtained by averaging the spectra of the eight targets covering the spectral range between [O II]  $\lambda 3727$  and [O III]  $\lambda 5007$ . The lower panel shows the number of spectra used for each pixel, as the pixels interested by bright sky lines were not included. The positions of the undetected lines [Ne III]  $\lambda 3869$  and He I 3889 are shown for reference.

excludes that the ionization could be dominated by an AGN. The [O II]  $\lambda 3727$  line is outside the observed range and the [O III]  $\lambda 5007$  line is barely detected as it is coincident with a sky line. As a consequence we cannot measure the metallicity of this object.  $H\beta$  is well detected in a clean part of the spectrum, and the  $H\alpha/H\beta$  ratio is  $4.9 \pm 1.5$ , significantly above the case B value of 2.85. Assuming that this difference is due to a screen of dust following the Cardelli, Clayton & Mathis (1989) extinction law, we derive  $A_{V,el} = 1.7$ . This is consistent with what is derived by the spectral fitting,  $A_{V,c} = 1.1$ . MD 19 is very extended both in UV and in  $H\alpha$ . The stellar continuum of this object is clearly detected and appears to be displaced from the peak of the lines.

### 5.6 Q0302–C131

This galaxy is elongated both in line and UV images, with a shape reminding a classical edge-on disc. The position angle of the elongation in the line image is fully consistent with that in the UV image. Most of the lines are in a clean part of the spectrum, only the [Ne III]  $\lambda 3869$  line is hidden by a sky line.

### 5.7 Q0302–M80

In the broad-band image this galaxy is very extended, with an elongated structure. In contrast, the line image appears very compact and regular. Both [O II]  $\lambda 3727$  and [Ne III]  $\lambda 3869$  fall near bright sky lines and cannot be detected.

### 5.8 Q0302–C171

This is the object with the faintest [O III]  $\lambda 5007$ . While most of the main emission lines are not strongly affected by sky lines, the flux of [O II]  $\lambda 3727$  is very uncertain because the line falls near a bright sky line at  $1.613 \mu m$ .

## 5.9 Composite spectrum

The average spectral properties of the LSD galaxies can be better shown by constructing an average spectrum. Furthermore, fainter spectral features, below detection in any single spectrum, could be revealed by summing up all the spectra. Fig. 4 shows the average, composite spectrum of the eight LSD sources whose spectra cover the [O II]  $\lambda 3727$ –[O III]  $\lambda 5007$  region. This spectrum was obtained as an average of the original ones without any weighting, and reveals the average properties of the LSD sample as if they were observed simultaneously. Large [O III]  $\lambda 5007/H\beta$  and [O III]  $\lambda 5007/[O II] \lambda 3727$  ratios relative to local galaxies are shown, and this is related to metallicity as explained in Section 4.6. The corresponding average mass is  $\log(M_*/M_\odot) = 9.80$ .

## 6 ANALYSIS

In the previous sections we have measured stellar mass, SFR, metallicity and size of our sample of LBGs. In this section we intend to use these parameters to derive information on the history and evolutionary state of these galaxies. We will show that mass–metallicity relation, gas masses and effective yields can provide important clues on the physical processes dominating the evolution of these objects and on the relation between these starburst and similar objects at lower redshifts.

### 6.1 The mass–metallicity relation

Fig. 5 shows the stellar mass–metallicity relation at  $z \sim 3.1$ , compared to the same relation as measured at lower redshifts. All the presented data have been scaled to a Chabrier (2003) IMF and use the same metallicity calibration. A strong, monotonic evolution of metallicity can be seen, i.e. galaxies at  $z \sim 3.1$  have metallicities  $\sim$ six times lower than galaxies of similar stellar mass in the local universe. It is worth noticing that this is not the evolution of

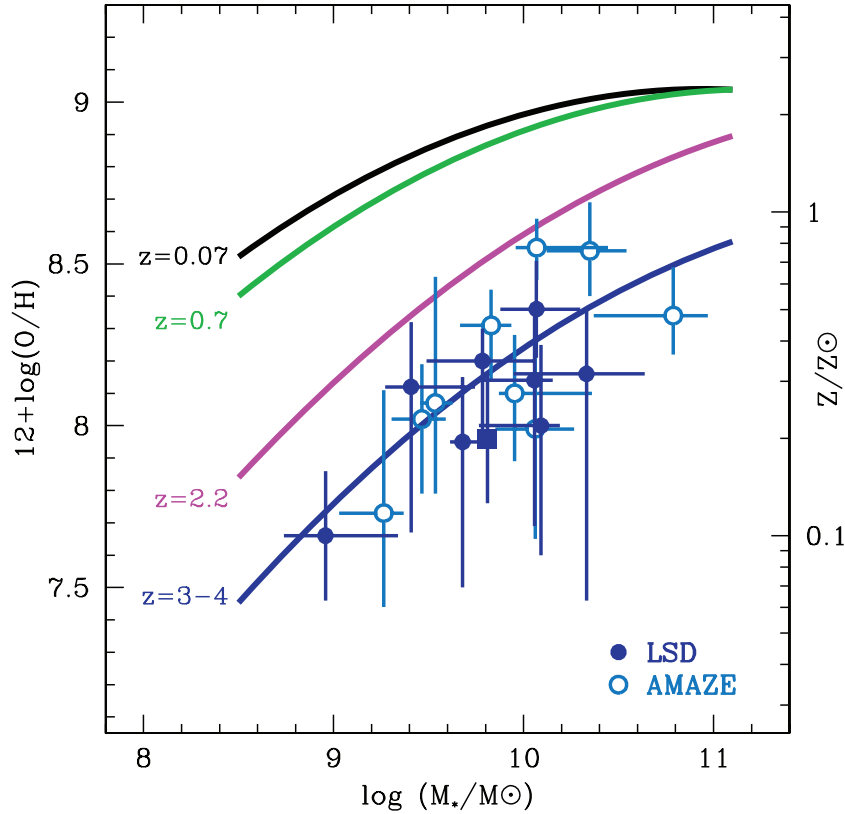


**Figure 5.** Evolution of the mass–metallicity relation from  $z = 0.07$  (Kewley & Ellison 2008) to  $z = 0.7$  (Savaglio et al. 2005),  $z = 2.2$  (Erb et al. 2006a) and  $z = 3-4$  (AMAZE+LSD). All data have been calibrated to the same metallicity scale and IMF (Chabrier 2003) in order to make all the different results directly comparable. Turquoise empty dots show the AMAZE galaxies, blue solid dots the LSD galaxies. The solid square shows the ‘average’ LSD galaxy, having average mass and composite spectrum (see Fig. 4). The lines show quadratic fits to the data, as described in the text.

individual galaxies, as discussed in Maiolino et al. (2008), but this is the evolution of the average metallicity of the galaxies contributing to a significant fraction of the SF activity at their redshifts. The observed evolution implies that galaxies with relatively high stellar masses [ $\log(M/M_\odot) = 9-11$ ] and low metallicity are already in place at  $z > 3$ , and this can be used to put strong constraints on the processes dominating galaxy formation.

While stellar mass, based on integrated photometry, is representative of the full galaxy, metallicity is possibly dominated by the central, brightest regions. The presence of metallicity gradients could have some influence on the observed mass–metallicity relation. These aperture effects are present at any redshift: even at  $z \sim 0$ , galaxy spectra from Sloan Digital Sky Survey (SDSS) refer to the central few arcsec of the galaxies. In most models, the central brightest part of the galaxies are also the most metal rich, therefore, the use of total metallicities for our LSD galaxies is expected to produce an even larger evolution.

The effect of ‘downsizing’ (Cowie et al. 1996) on chemical enrichment is expected to produce differential evolution related to stellar mass. Stronger evolution for low-mass galaxies is observed from  $z = 0$  to 2.2 (see Fig. 5). The observed spread of the distribution and the uncertainties on the single points still make it impossible to see if such an effect is already in place between  $z = 2.2$  and 3–4. Constraints on this effect can be derived when the full AMAZE data sample will be presented.

Using the same representation as in Maiolino et al. (2008), we fit the evolution of the mass–metallicity relation with a second-order

polynomial:

$$Z = A[\log(M_*) - \log(M_0)]^2 + K_0,$$

where  $A = -0.0864$  and  $M_0$  and  $K_0$  are the free parameters of the fit. By using the LSD and AMAZE galaxies, we derive  $\log(M_0) = 12.28$  and  $K_0 = 8.69$ . The values of  $M_0$  and  $K_0$  for the samples at lower redshifts can be found in Maiolino et al. (2008), and can be converted to the present system by subtracting  $\log(1.7)$  to  $M_0$ .

Several published models of galaxy formation (e.g. de Rossi, Tissera & Scannapieco 2007; Kobayashi, Springel & White 2007) cannot account for such a strong evolution. The physical reason for this can be due to some inappropriate assumption, for example about feedback processes or merging history. When taken at face value, some other models (e.g. Brooks et al. 2007; Tornatore et al. 2007) provide a better match with the observations, but a meaningful comparison can only be obtained by taking into account all the selection effects and observational biases, and by comparing not only stellar mass and metallicity but also all the other relevant parameters, such as dynamical mass, angular momentum, gas fraction, SFR, morphology and size (see, for example, Calura et al. 2009).

In fact, it is important to emphasize that the galaxy samples used for Fig. 5 change with redshift. In the Tremonti et al. (2004) work, the local SDSS galaxies under study constitute an almost complete census of the local star-forming galaxies, and the derived mass–metallicity relation shows the average properties of the sample. At

high redshift, especially at  $z > 1$ , a number of effects must be considered. Only the most active galaxies are selected, and the observed metallicity refer to these objects. If, for example, less active, already formed and enriched galaxies are present at  $z = 3$ , they would not be present in our sample; the fraction of galaxies selected is likely to change with mass, and this is expected to introduce some systematic effect with stellar mass; the rest-frame UV selection misses extinguished galaxies, therefore, an increasing fraction of dusty, metal-rich galaxies are excluded from the mass–metallicity relation at high metallicities; the *UGR* colour–colour selection for the LBGs excludes galaxies with red ( $G - R$ ) colours due to the presence of older stellar populations. For example, Hayashi et al. (2008) observed a sample of *K*-selected, star-forming galaxies at  $z \sim 2$ . They found a mass–metallicity relation which is similar to that in Erb et al. (2006a) but with an offset of about 0.2 dex towards higher metallicities. The difference is likely to be due to target selection. Evolution in the mass–metallicity plane can also be produced by different SF histories of individual galaxies: if, for example, each galaxy experiences several bursts of star formation, galaxies detected during the first burst will show low stellar masses and low metallicities, while galaxies with the same baryonic and total masses but detected during later bursts will show higher metallicities and stellar masses. This is not the case if galaxies have only one major burst, and all the galaxies are selected during the same phase.

All these effects are present at any redshift but their importance changes significantly among the different samples. For this reasons, the quantitative interpretation of the observed evolution requires great care. A meaningful comparison between a sample of galaxies caught during a special phase of their life at  $z = 3$ , with a more representative sample of galaxies at  $z = 0$  can only be done when the selection effects are taken into account. This will be the subject of a future work.

## 6.2 SFR and stellar mass

Several studies of galaxies have found a correlation between stellar mass  $M_*$  and SFR, i.e. more massive galaxies also have larger SFRs (see, for example, Schiminovich et al. 2007 for a UV-selected sample, Elbaz et al. 2007 for an optical-selected sample and Daddi et al. 2007 for a *K*-band-selected sample). In contrast, local ultraluminous infrared galaxies (ULIRG) do not follow the same relation but lie above it (Elbaz et al. 2007). The slope of the correlation is not well constrained. While some authors (Daddi et al. 2007) find SFRs proportional to  $M_*$ , i.e. specific SFR ( $\text{SSFR} = \text{SFR}/M_*$ ) constant with mass, in most cases a much weaker dependence of SFR on  $M_*$  is found (Noeske et al. 2007; Zheng et al. 2007; Drory & Alvarez 2008). Other authors find an evolution of the slope with redshift (Dunne et al. 2008), while in some samples the SFR seems to be more directly related to stellar surface density rather than stellar mass (Franx et al. 2008).

The existence of such a relation and its slope are strongly affected by sample selection. For example, colour-based selections tend to generate some proportionality between  $M_*$  and SFR because stronger SFRs are needed to significantly affect the colours of more massive galaxies. For UV-selected galaxies with SFRs estimated from the optical emission lines, similar to LSD, at  $z \sim 2$  Erb et al. (2006a) have found a positive, albeit weak, correlation between  $M_*$  and SFR by removing the galaxies which have dynamical mass much higher than the stellar mass. In contrast, the SINS sample (Förster Schreiber et al. 2009) shows a much stronger

dependence of SFR on  $M_*$  with slope consistent with one, in agreement with the correlation found for the *K*-band-selected sample in Daddi et al. (2007).

To produce such a correlation, galaxies must spend a large portion of their life forming stars at a characteristic fractional level, instead of forming most of their stellar mass in a few large bursts. As a consequence, this correlation is often interpreted as an evidence that most of the SF activity is not related to short, intense burst but rather is associated to a more continuous activity at a lower level. This is confirmed, at  $z \sim 2.2$ , by the fact that the current SFR in Erb et al. (2006b) is similar to the past average. This ongoing activity could be related to cold accretion of gas followed by disc instabilities (Dekel & Birnboim 2006; Dekel, Sari & Ceverino 2009). The regular morphologies of the galaxies dominating the SF activity at intermediate redshifts (Bell et al. 2005; Wolf et al. 2005) and the (generally) regular dynamics observed at  $z \sim 2$  (Förster Schreiber et al. 2006; Genzel et al. 2008; Shapiro et al. 2008; Stark et al. 2008) support this interpretation.

It is interesting to study if a correlation is present in our sample, and Fig. 6 shows the relation between  $M_*$  and SFR in the LSD sample. Large uncertainties are present, in particular on the SFR that is very sensitive to the poorly constrained amount of dust extinction. The LSD galaxies appear to have SFRs and  $M_*$  similar to the lower redshift galaxies in the samples mentioned above, but the small number of data points and the large intrinsic errors makes it impossible to obtain robust conclusions about the existence of a correlation.

It is important to study if selection effects could hide a strong correlation between  $M_*$  and SFR. The rest-frame UV selection explains why no galaxy below a given SFR threshold is selected. On the contrary, the lack of active, massive could be due to several effects: (1) high-mass galaxies selected as LBGs with high SFRs could be rare objects, and therefore none of them is included in this sample of 10 objects; (2) it is possible that the dust content of the galaxies increases with age and metallicity, i.e. with stellar mass. In this case massive galaxies with large SFRs could be too red or too faint in the UV to be selected as LBGs, and could be present in other catalogues as submm galaxies or ULIRGs. For example, this is what is observed by Nesvadba et al. (2007) in the archetypal submm galaxy SBS J14011+0252, which is both metal rich, actively star forming and dusty; (3) the SF activity of each galaxy could be a decreasing function of time, with a strong burst followed by a rapid decrease. In this case massive galaxies would also have low SFRs.

Albeit these limitations, our data do not support the existence of an almost direct proportionality ( $\text{SFR} \sim M_*^{1.0}$ ) between SFR and  $M_*$  similar to that in Daddi et al. (2007) and Förster Schreiber et al. (2009). In contrast, we find better agreement with a flatter relation ( $\text{SFR} \sim M_*^{0.3}$ ) as found by Erb et al. (2006a). This implies the presence of larger SSFRs in lower mass galaxies. As shown by the dashed lines in Fig. 6, the same effect can be expressed by the SF time-scale, defined as the time  $t_*$  to form the present amount of stars  $M_*$  at the present level of SF,  $t_* = M_*/\text{SFR} = 1/\text{SSFR}$ . In the LSD sample,  $t_*$  changes systematically with  $M_*$ : low-mass galaxies have  $t_* \sim 10^8$  yr, while higher mass galaxies have  $t_* \sim 10^9$  yr. This is an indication that, in relative terms, the current episode of SF is more important in lower mass systems. While high-mass galaxies have SFRs and SSFRs similar to what observed at lower redshift, low-mass galaxies tend to be relatively more active. This interpretation implies that less massive galaxies are also younger. An accurate test of this prediction is not easy, as it is difficult to measure the age of high-redshift galaxies. Nevertheless, it is consistent with

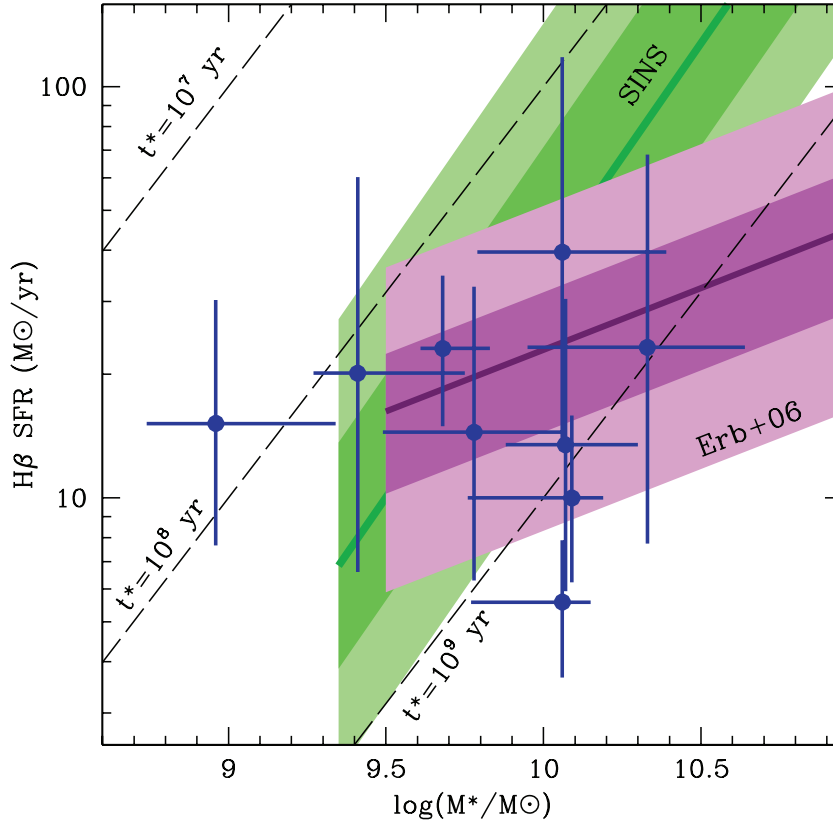


**Figure 6.** SFR as a function of stellar mass for the galaxies in the LSD sample. This distribution is compared with two observed correlations at lower redshift ( $z \sim 2$ ), in magenta the UV-selected sample by Erb et al. (2006b), in green the SINS galaxies (Förster Schreiber et al. 2009). The thick lines show the median of the correlations, while the colour-shaded regions are delimited by the 5, 25, 75 and 95 per cent percentiles of each distribution. Compared to the sample at  $z \sim 2$ , LSD galaxies show a larger dispersion. The long-dashed lines show some values of SF time-scales, defined as  $t_* = M_*/\text{SFR}$ . LSD galaxies have SF time-scales between  $10^8$  and  $10^9$  yr.

the broad correlation between stellar mass and age described in Section 4.3.

### 6.3 The mass in gas

In local star-forming galaxies, the surface density of SF  $\Sigma_{\text{SFR}}$  is related to the surface density of gas  $\Sigma_{\text{gas}}$ :

$$\Sigma_{\text{SFR}} \propto \Sigma_{\text{gas}}^n.$$

This is the Schmidt–Kennicutt law (see, for example, Kennicutt 1998), which seems to be already in place at high redshifts (Bouché et al. 2007). It is interesting to note that downsizing is a natural consequence of the Schmidt law and of the other scaling relations, as shown by Erb (2008). If infalls and outflows can be neglected on the time-scale of a starburst, or if they are proportional to the SFR itself, the Schmidt law produces a decreasing SFR whose initial, maximum value scales with the mass  $M$  and the size  $r$  as  $M^{1.4}r^{-0.8}$ , and the typical time-scales as  $M^{-0.4}r^{0.8}$ . If we assume that galaxies follow the same mass–size relation observed in the local massive, early-type galaxies by Shen et al. (2003), we obtain that the typical time-scale decreases with mass as  $M^{-0.1}$  and, correspondingly, the magnitude of the initial starburst increases as  $M^{1.1}$ . The typical time-scales computed by Erb (2008) are  $\sim 0.3$  Gyr for  $M = 10^{12} M_\odot$ , and  $\sim 4$  Gyr for  $M = 10^9 M_\odot$ .

The Schmidt–Kennicutt law is often used to estimate gas density and gas mass starting from the observed SFR and galaxy size (for example, Erb et al. 2006a; Erb 2008). The slope  $n$  of the relation is

still uncertain. The ‘classic’ value of  $n$  is 1.4, given by Kennicutt (1998). SF due to large-scale instabilities of the disc naturally produces  $n = 1.5$  (Elmegreen 2002), and such a value is supported by more recent observations (Kennicutt et al. 2007) on small scales. In high redshift studies, Bouché et al. (2007) found a slightly larger value,  $n = 1.7$ , a value which depends on the adopted value of the CO/H<sub>2</sub> ratio. Such a value could be more appropriate for our LBGs, nevertheless for consistency with previous works we adopt the relation in Kennicutt (1998), deriving the following equations for the gas surface density  $\Sigma_{\text{gas}}$  and the gas mass  $M_{\text{gas}}$ , valid when the Chabrier (2003) IMF is used:

$$\Sigma_{\text{gas}}(M_\odot \text{ pc}^{-2}) = 254 \left( \frac{\text{SFR}}{M_\odot \text{ yr}^{-1}} \right)^{0.71} \left( \frac{r}{\text{kpc}} \right)^{-1.42}, \quad (1)$$

$$M_{\text{gas}}(M_\odot) = 798 \left( \frac{\text{SFR}}{M_\odot \text{ yr}^{-1}} \right)^{0.71} \left( \frac{r}{\text{kpc}} \right)^{0.58}. \quad (2)$$

Using the values in Bouché et al. (2007) would result in gas fractions about 40 per cent lower, which however do not affect the conclusions of this work.

The largest uncertainties in these equations are related to the half-light radius  $r$ , which has large errors, as explained above. This is important for  $\Sigma_{\text{gas}}$ , which has a strong dependence on galaxy size. In contrast, the total gas mass  $M_{\text{gas}}$  is much less sensitive to galaxy size as it depends on  $r^{0.58}$  and, as a consequence, the uncertainties on this quantity are smaller.

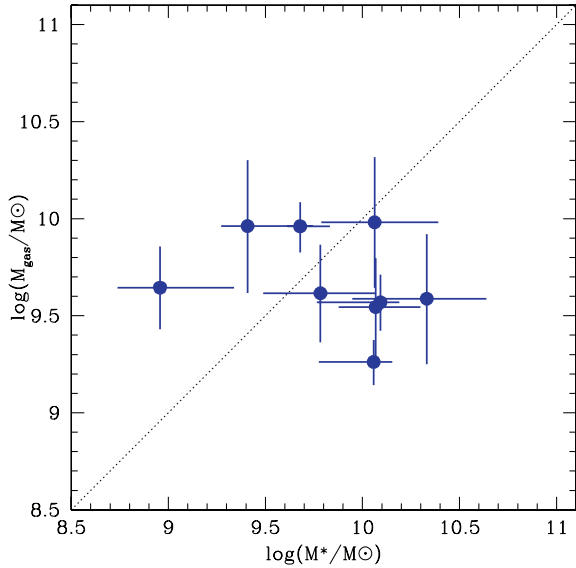


**Figure 7.** Mass of gas as a function of the stellar mass for the LSD galaxies. The dotted lines show equal masses. All the galaxies have similar amount of gas, which is not related to stellar mass.

The observed SFR densities are between  $0.5$  and  $6 M_{\odot} \text{ yr}^{-1} \text{ kpc}^{-2}$ , similar to what observed both in the local universe (Kennicutt 1998) and at  $z = 2.2$  (Erb et al. 2006b). The corresponding gas densities range between  $300$  and  $2000 M_{\odot} \text{ pc}^{-2}$ , similar to the values derived for LBGs and ULIRGs by Coppin et al. (2007) and Tacconi et al. (2006). As we are sampling the central, most active part of the galaxies, these numbers must be considered as the maximum surface densities of gas.

Fig. 7 shows the resulting  $M_{\text{gas}}$  as a function stellar mass. It is evident that gas mass does not correlate with  $M_*$  and that  $M_{\text{gas}}$  covers a much smaller range than  $M_*$ . While the largest galaxy has a stellar mass 24 times larger than the smallest, the most gas-rich galaxy has only five times more gas than the poorest. This result could be partly due to a combination of selection effects and spatial resolution. As all the galaxies have similar SFRs, the range in gas mass can be dominated by the range in intrinsic dimensions. Our resolution,  $0.2$  arcsec FWHM, corresponding to about  $1.4$  kpc, is similar to the intrinsic galaxy size. As a consequence, it is possible that we are overestimating the size, and therefore the gas mass, of the smallest galaxies.

Interesting information on the physical properties of the LSD galaxies can be obtained by comparing the different time-scales. We have already introduced the *stellar* time-scale  $t_*$ , which measures the time to create the observed amount of stars at the current SFR. The typical *dynamical* time-scale is  $t_{\text{dyn}} = 2\pi R^{3/2}/(GM)^{1/2}$ , where  $R$  is the typical radius and  $M$  the typical total mass. Any starburst activity is expected to last at least  $t_{\text{dyn}}$  (Dekel & Birnboim 2006). The LSD galaxies have  $t_{\text{dyn}}$  between  $0.4$  and  $1.0 \times 10^8$  yr. This narrow range of values is not surprising, because if size depends on mass as in local early-type galaxies, dynamical times are almost independent of mass. A third important time-scale is the *gas exhaustion* time  $t_{\text{ex}}$ , i.e. the time to exhaust all the available gas at the current rate of SF,  $t_{\text{ex}} = M_{\text{gas}}/\text{SFR}$ . For the LSD galaxies, this spans a narrow range, between  $3$  and  $6 \times 10^8$  yr.

We have already seen that  $M_{\text{gas}}/M_*$ , and therefore  $t_*/t_{\text{ex}}$ , varies systematically with  $M_*$ , meaning that the smallest galaxies are more gas rich and are forming a larger fraction of stars. The ratio between  $t_{\text{dyn}}$  and  $t_{\text{ex}}$  ranges between  $6$  and  $4$ , with no clear dependence on

$M_*$ . This implies that the galaxies are so gas rich that the current level of SF can be sustained for several  $t_{\text{dyn}}$ . We cannot be sure that the SF activity will proceed for so long, but this is an indication that we are dealing with major episodes of SF in galaxies which have accreted large amounts of gas, of the order of  $10^{10} M_{\odot}$  (see Fig. 7). In these galaxies SF follows mass assembly.

#### 6.4 The fraction of gas

The gas mass  $M_{\text{gas}}$  can be compared with the total baryonic mass  $M_b$  to estimate the fraction of mass in gas, an indication of the evolutionary stage of the galaxy. The results are shown in Fig. 8, where the gas fraction is plotted versus the stellar mass. It should be noted that stellar and gas masses are not measured in the same apertures. When *HST* images for these objects are available (see Section 3.2), we will be able to quantify this effect and apply a correction. Despite the large uncertainties, a clear correlation is seen between stellar mass and gas fraction. This is similar to what is observed at low redshifts, where a tight correlation exists between gas fraction and rotation velocity (Dalcanton 2007) or stellar mass (Bell 2003; Kannappan 2004). The same effect is also observed by Erb et al. (2006a) and Reddy et al. (2006) in their samples at  $z \sim 2$ . The relation between stellar mass and gas fraction in local galaxies is often used to constrain the models of galaxy formation (e.g. Somerville et al. 2008).

The observed correlation is at least partly due to the selection effects of our target sample, shown as a grey-shaded area. As explained above, our sample is selected according to the SFR, while stellar mass can assume a wide range of values. The existence of this selection effect makes it impossible to test at  $z = 3$  the results of several models of galaxy formation, such as Brooks et al. (2007) and Mouchine et al. (2008). These models predict that a strong correlation exists between  $f_{\text{gas}}$  and  $M_*$  at any redshift, with more massive galaxies having a lower content in gas, very similar to what

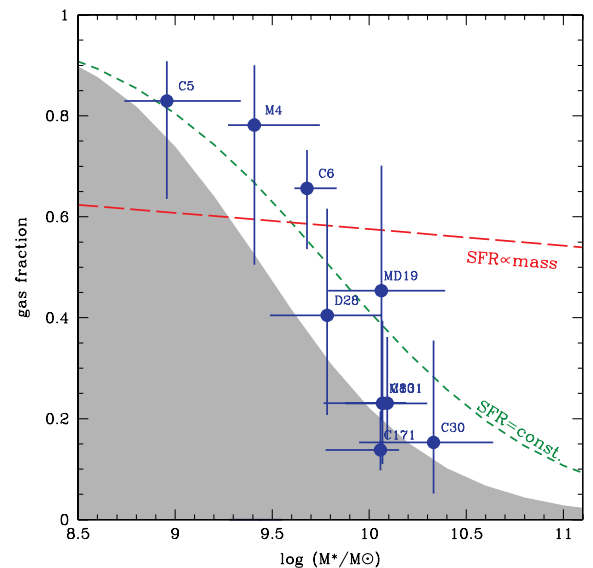


**Figure 8.** Fraction of baryonic mass in gas as a function of stellar mass. The blue solid dots are the LSD galaxies. The grey-shaded area represents galaxies that cannot be included in our sample because the SFR is lower than our limit ( $\sim 15 M_{\odot} \text{ yr}^{-1}$ ). The dashed lines show the expected dependence of gas fraction on stellar mass for galaxies having SFR constant (green) or proportional to the stellar mass (red).

is actually observed (see also Calura et al. 2008). In other words, the shaded region in Fig. 8 could be empty for physical reasons.

The *expected* gas fraction as a function of stellar mass can be derived once the dependence of dimensions and SFR on  $M_*$  is known. We compute this gas density using the mass–size relation for massive, late-type galaxies in Shen et al. (2003),  $r \propto M^{0.4}$ , and assuming that the SFR of the galaxies does not depend on stellar mass. As size is expected to change slowly with mass, these results are largely independent of the evolution of the mass–size relation, which is largely unknown. The result is plotted as a short-dashed, green line in Fig. 8. In contrast, assuming that the SFR is proportional to stellar mass as observed in the local universe (see Section 4.5), we derive the long-dashed, red line in the same figure. The normalization of these two lines can vary as a function of the adopted SFR and galaxy size, but the shape of the curves show that the gas fraction measured in our target galaxies is that expected for an SFR-limited sample.

### 6.5 The effective yields

Important hints on the physical processes shaping the mass–metallicity relation can be obtained by considering the effective yields, i.e. the amount of metals produced and retained in the ISM per unit mass of formed stars (Garnett 2002; Dalcanton 2007). In a closed-box model, metallicity  $Z$  (i.e. the mass in metals divided by the mass of the interstellar gas) can be written as a simple function of the gas fraction  $f_{\text{gas}}$ :

$$Z = y \ln(1/f_{\text{gas}}), \quad (3)$$

where  $y$  is the true stellar yield, i.e. the ratio between the amount of metals produced and returned to the ISM and the mass of stars. This is the solution of a differential equation (see Edmunds 1990) valid in a closed-box case, with instantaneous recycling, instantaneous mixing and low metallicities. The solar yield  $y_{\odot}$ , i.e. the fractional contribution of metals to the solar mass, is often used as reference and is 0.0126 (Asplund et al. 2004). By inverting this equation, and using observed quantities for  $Z$  and  $f_{\text{gas}}$ , we obtain the *effective* yields:

$$y_{\text{eff}} = Z / \ln(1/f_{\text{gas}}). \quad (4)$$

The measured values of  $y_{\text{eff}}$  could differ from the true stellar yields  $y$  if some of the assumptions used to derive equation (3) do not hold, in particular if the system is not a closed box. Outflows of very enriched material, such as the ejecta from SNe, extract metals, decreasing  $Z$ , while infalls of pristine gas can increase  $f_{\text{gas}}$  and decrease  $Z$ . It is well known that both effects must be present at some level. Gas infall, either in merging episodes or in cold gas accretion, is needed to supply galaxies with the amount of matter we observed in stars today, while starbursts are known to produce SN driven winds of the order of  $0.1 M_{\odot} \text{ yr}^{-1} \text{ kpc}^{-2}$  (Lehnert & Heckman 1996a). The presence of both effects does not imply that both contribute significantly to the chemical evolution of the systems and, in particular, to the observed yields. In all cases,  $y_{\text{eff}}$  must be smaller than  $y$ , as discussed, for example, by Edmunds (1990) and Dalcanton (2007). This is why it is interesting to measure the effective yields, because it can measure how a system is far from being a closed box.

In the local universe, Tremonti et al. (2004) have found a significant dependence of  $y_{\text{eff}}$  on mass, i.e. lower mass galaxies have lower  $y_{\text{eff}}$ . The reduction of  $y_{\text{eff}}$  below the solar value  $y_{\odot}$  in galaxies

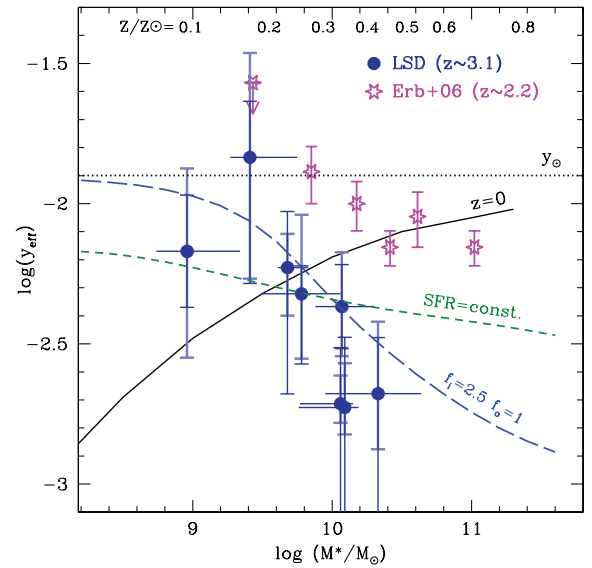


**Figure 9.** Effective yields of the LSD sample (solid blue dots), as a function of stellar mass, compared with the solar value (dotted line). Light and dark error bars show the contribution to the errors on yields due to the uncertainties on gas fraction and metallicity, respectively. The magenta stars are the results by Erb et al. (2006a) at  $z = 2.2$ . The black solid line is the local results by Tremonti et al. (2004). The green dashed line corresponds, as in Fig. 8, to galaxies with constant SFR. The blue, long-dashed line is the model with infalls and outflows proportional to the SFR described in the text. The labels near the top of the figure show the values of the average metallicity for galaxies of a given stellar mass as derived from the mass–metallicity relation.

with low stellar mass is usually described as a consequence of outflows. If outflows are the main effect shaping the mass–metallicity relation, then the effective yields are expected to increase with stellar mass because lower mass galaxies, having a shallower potential well, have lost a larger fraction of metals into the IGM. Above a certain stellar mass, the galaxy potential well is too deep for the SNe to eject significant fraction of enriched gas, and  $y_{\text{eff}} \sim y$  is expected in massive galaxies.

Fig. 9 shows the values of  $y_{\text{eff}}$  for the LSD galaxies. The errors on each single point are large, as they reflect the large uncertainties on both gas fractions and metallicities. Systematic effects on dimensions could also be present, as discussed above. Nevertheless, the situation seems pretty clear: rather than *increasing* with stellar mass toward solar values, in the LSD sample  $y_{\text{eff}}$  is found to *decrease* with stellar mass, starting from  $y_{\odot}$  at the low-mass end. The differences with the results by Tremonti et al. (2004) are striking. This is not surprising because it means that the physical processes dominating the SDSS galaxies in the local universe are not the same as in LBGs at  $z > 3$ . In contrast, our result is very similar to what has been found by Erb et al. (2006a). Our and Erb’s samples share the same dependence of  $y_{\text{eff}}$  with stellar mass, although LSD galaxies have lower  $y_{\text{eff}}$  because of their lower metallicity. Our results are also similar to those of Weiner et al. (2008) at  $z = 1.4$  and Law et al. (2007) at  $z = 2.5$ , who detected the presence of stronger galactic winds in more massive galaxies.

To interpret this result we have to take into account how the samples were chosen and the scaling relations. From the *expected* gas fraction in Fig. 8 and the mass–metallicity relation in Fig. 5, we can *predict* the  $y_{\text{eff}}$  of the LSD sample. This is a real prediction, i.e. once you define SFRs, metallicity and dimensions, there are no free parameters to compute yields. We plot this prediction in Fig. 9. The



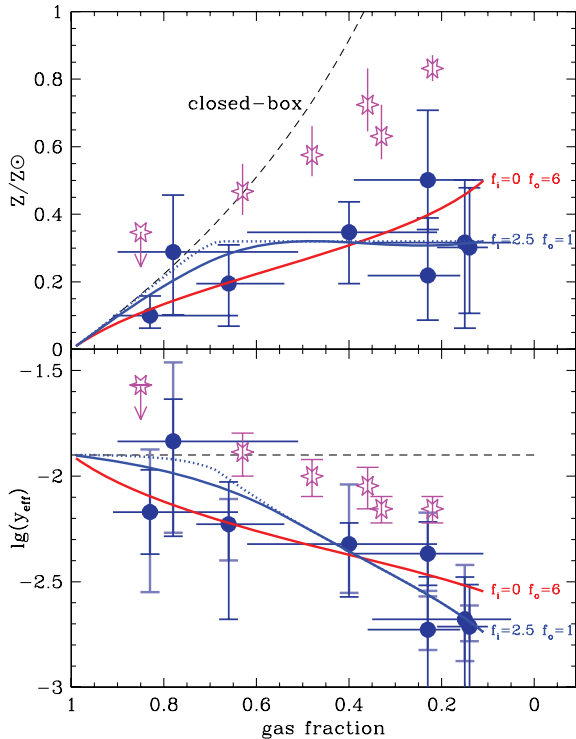


**Figure 10.** Metallicity (top) and effective yields (bottom) as a function of gas fraction. This is plotted decreasing rightwards, to have galaxies evolving from left to right. The blue solid dots are the LSD galaxy sample, the magenta stars the Erb et al. (2006a) data. The black dashed line shows the expectations from a closed-box model. The solid lines show the results of applying the model in Erb (2008) with values of  $f_i$  and  $f_o$  in the labels. The red line shows a model with pure outflows, with ejected mass six times the SFR. The blue line is a model with both infall ( $f_i = 2.5$ ) and outflow ( $f_o = 1$ ). The blue dotted line is this same model but without outflow ( $f_i = 2.5$  and  $f_o = 0$ ).

observed behaviour is in agreement with what is expected for an SFR-limited sample. In other words, the dependence of the yields on stellar mass is a direct consequence of the mass–metallicity relation and of the other scaling relations.

The presence of yields decreasing with mass implies that the classical outflows, whose specific power decreases with increasing galaxy mass, do not apply to the LBG at  $z \sim 3.1$ . The mass–metallicity relation at  $z > 3$  must have a different origin.

The dependence of  $y_{\text{eff}}$  on stellar mass is a secondary effect due to the relation between stellar mass and gas fraction. For this reason, the physical meaning of these findings is better understood by plotting  $y_{\text{eff}}$  directly as a function of gas fraction. This is done in Fig. 10. The relation between these two quantities and the effect of infalls and outflows are described by several authors. In particular, Dalcanton (2007) shows that outflows of very enriched materials can be very effective in reducing  $y_{\text{eff}}$ , especially for gas-rich systems. Gas-poor system can change their  $y_{\text{eff}}$  by a factor of 2, as observed in the LSD galaxies, if they accrete a significant amount of gas, larger than the internal gas.

For gas-rich systems,  $y_{\text{eff}}$  does not depend on  $f_{\text{gas}}$  and it is equal to the stellar yields  $y$  (Dalcanton 2007), thus allowing us to measure this quantity, which in principle could be different from  $y_{\odot}$ . Metallicity can influence nucleosynthesis in different ways. The most important effect is expected to be mass loss, which has a strong dependence on metallicity. Massive stars with stronger stellar winds lose a larger fraction of He and C that would otherwise be converted

to O. As a consequence, the oxygen yield we measure is expected to decrease with metallicity. The expected effect is not large, up to a factor of 2, but in principle measurable with our data (Woosley & Weaver 1995; Marigo 2001; Garnett 2002). All the LSD galaxies with  $f_{\text{gas}} > 0.7$  have  $y_{\text{eff}}$  fully consistent with  $y_{\odot}$ , showing that any metallicity dependence of  $y$  is not large even at  $Z \sim 0.1 Z_{\odot}$ .

Matteucci (2001) (see also Matteucci 2008) and Erb (2008) introduce a model in which galaxies have infalls and outflows proportional to the SFR. The instant recycling and mixing approximations are used, infalling gas is assumed to have no metallicity, while the metallicity of the outflowing gas is considered to be the same as the ISM. This model can be used to reproduce  $y_{\text{eff}}$  by changing two free parameters, i.e. the amount of infall  $f_i$  and outflow  $f_o$  in unit of the SFR of the galaxy. Two more parameters can be varied, if necessary, i.e., the true yield  $y$ , and the fraction  $\alpha$  of mass still locked in stars. Implicitly, the physical properties of these outflows differ significantly with what is invoked to explain the yields in the local universe: given the correlation between SFR and  $M_*$  (Erb et al. 2006b; Schiminovich et al. 2007), at  $z \sim 2$  these outflows are expected to increase, rather than decrease, with stellar mass. Erb et al. (2006a) and Erb (2008) find that their data at  $z = 2.2$  can be adequately reproduced by a supersolar true yield ( $y = 1.5 y_{\odot}$ ) and significant infalls and outflows, with the best-fitting parameters of  $f_i = 2.2$  and  $f_o = 1.3$ .

We have applied this model to LSD, reproducing the dependence of  $y_{\text{eff}}$  on  $f_{\text{gas}}$  varying  $f_i$  and  $f_o$ . Infalls are effective in changing  $y_{\text{eff}}$  for the gas-poor galaxies, leaving gas-rich galaxies much more unaffected. Outflows are more efficient in reducing  $y_{\text{eff}}$  in gas-rich galaxies, and much less effective for gas-poor galaxies. In contrast to Erb (2008), we have fixed the values of  $y$  to  $y_{\odot}$ , as explained above. The parameter  $\alpha$  is a slowly decreasing function of time, as more stars leave the main sequence, but can vary in quite a small range. It is expected to be  $\sim 0.93$  at  $t = 10^7$  yr,  $\sim 0.84$  at  $t = 10^8$  yr,  $\sim 0.76$  at  $t = 10^9$  yr and approaching 0.60–0.65 after a Hubble time (Bruzual & Charlot 2003). Given the ages of our galaxies, we have used  $\alpha = 0.8$ , and the results are not very sensitive to the value chosen. The results are shown in Fig. 10. Outflows without infalls can explain the observed  $y_{\text{eff}}$ , but in this case large values of  $f_o$  between 4 and 8 are needed. The figure shows the best-fitting pure outflow model, having  $f_o = 6$ . In other words, if pure outflows are responsible for the reduction of  $y_{\text{eff}}$ , the most active galaxies must eject into the IGM masses of the order of  $400\text{--}800 M_{\odot} \text{ yr}^{-1}$ , while converting  $100 M_{\odot} \text{ yr}^{-1}$  into stars. This must happen in galaxies as massive as  $3 \times 10^{10} M_{\odot}$ , i.e. galaxies that, in the local universe, show solar yields. As a comparison, Weiner et al. (2008) found outflowing masses of about  $20 M_{\odot} \text{ yr}^{-1}$  in their sample of starburst galaxies at  $z = 1.4$ , whose SFRs are  $10\text{--}100 M_{\odot} \text{ yr}^{-1}$ , similar to the present sample. Pure infalls can explain the yields with lower amount of flowing gas. In this case, the best-fitting value is  $f_i = 2.5$ , with an acceptable range between  $f_i = 1.5$  and  $3.5$ . Once an infall with  $f_i \sim 2$  is present, it dominates the behaviour of  $y_{\text{eff}}$  and  $f_o$  can assume any value between 0 and 7. The best-fitting model with  $f_i = 2.5$  and  $f_o = 1$  is also plotted in Fig. 9 as a function of stellar mass, providing a good fit.

## 7 SUMMARY AND CONCLUSIONS: A PICTURE OF LBGs

We have obtained deep, spatially resolved, near-IR spectroscopy of a complete sample of LBGs at  $z \sim 3$ , selected only to be near a bright foreground star needed to drive the adaptive optics system. These galaxies are expected to give an unbiased representation of

the Steidel et al. (2003) sample of LBGs. The detected optical lines give information on many aspects of these galaxies, and in this paper we have analysed the properties related to metallicity, stellar and gas mass and gas fraction.

A strong evolution of the mass–metallicity relation is found, i.e. LBGs at  $z \sim 3$  have metallicities between 0.1 and 0.5 solar. Assuming that the Schmidt–Kennicutt law is already in place at  $z \sim 3$ , we derive the properties of the gas. Large masses of gas ( $\sim 10^{10} M_{\odot}$ ) are present in these galaxies, as a result of recent episodes of gas accretion. The gas fraction is found to be anticorrelated with stellar mass, and this is possibly due to the UV selection of the sample. These results on gas mass and metallicity imply that, at these redshifts, LBGs are already massive but still metal poor. This means that mass assembling is occurring before SF, as observed in early-type galaxies at lower redshifts (e.g. Saracco et al. 2003, 2005; Daddi et al. 2005). Once the selection effects are accurately considered, this can be used to put constraints on the models of galaxy formation and evolution.

The time-scale to produce the observed stars at the current level of SF varies from  $\sim 10^8$  yr for the smallest systems to  $\sim 10^9$  yr for the galaxies with the largest stellar mass. In contrast, the time-scale to exhaust the available gas is less variable, and is comparable with the dynamical times of these systems.

The effective yields decrease with stellar mass and have solar values at the low-mass end. This is in contrast with what is observed in the local universe, and can be ascribed to recent accretion of metal-poor gas at a rate of the order of the current SFR. Stellar yields have solar values even at  $Z \sim 0.1 Z_{\odot}$ .

All these evidences show that the LBGs of our sample can be described as starbursts on several dynamical time-scales following major events of gas accretion, due either to gas infall or merging with gas-rich, metal-poor galaxies. Low-mass galaxies can be described as experiencing their first major burst of SF. More massive galaxies are more gas poor and have lower yields, as is expected when gas infall ignites a new episode of SF in an older galaxy. Outflows are probably present but do not dominate the chemical evolution of these systems, that is more easily driven by infalls.

These galaxies will soon be observed by *HST* at optical and near-IR bands. These data will complement our near-IR, spatially resolved spectroscopy in order to study the morphological and dynamical properties of these galaxies and obtain a complete picture of these LBGs.

## ACKNOWLEDGMENTS

We thank F. Eisenhauer and A. Modigliani for support during data reduction, and B. Kennicutt and T. Nagao for very useful discussions. We also thank the staffs of ESO, *Spitzer* and TNG for excellent service observing, and E. Daddi for having provided data in tabular form. This work was partially supported by the Italian Space Agency through contract ASI-INAF I/016/07/0, by INAF CRAM 1.06.09.10 and by NASA (*Spitzer*) grant number 1343503.

## REFERENCES

- Argence B., Lamareille F., 2009, *A&A*, 495, 759  
 Asplund M., Grevesse N., Sauval A. J., Allende Prieto C., Kiselman D., 2004, *A&A*, 417, 751  
 Baffa C. et al., 2001, *A&A*, 378, 722  
 Bell E. F., 2003, *ApJ*, 586, 794  
 Bell E. F. et al., 2005, *ApJ*, 625, 23  
 Bolzonella M., Miralles J.-M., Pelló R., 2000, *A&A*, 363, 476  
 Bonnet H. et al., 2004, *The Messenger*, 117, 17  
 Bouché N. et al., 2007, *ApJ*, 671, 303  
 Brinchmann J., Pettini M., Charlot S., 2008, *MNRAS*, 385, 769  
 Brooks A. M., Govorov F., Booth C. M., Willman B., Gardner J. P., Wadsley J., Stinson G., Quinn T., 2007, *ApJ*, 655, L17  
 Bruzual G., Charlot S., 2003, *MNRAS*, 344, 1000  
 Calura F., Jimenez R., Panter B., Matteucci F., Heavens A. F., 2008, *ApJ*, 682, 252  
 Calura F., Pipino A., Chiappini C., Matteucci F., Maiolino R., 2009, *A&A*, in press, (arXiv:0904.2180)  
 Calzetti D., Armus L., Bohlin R., Kinney A. L., Koornneef J., Storchi-Bergmann T., 2000, *ApJ*, 533, 682  
 Cardelli J. A., Clayton G. C., Mathis J. S., 1989, *ApJ*, 345, 245  
 Chabrier G., 2003, *PASP*, 115, 763  
 Chapman S. C., Blain A. W., Smail I., Ivison R. J., 2005, *ApJ*, 622, 772  
 Conselice C. J. et al., 2007, *MNRAS*, 381, 962  
 Coppin K. E. K. et al., 2007, *ApJ*, 665, 936  
 Cowie L. L., Barger A. J., 2008, *ApJ*, 686, 72  
 Cowie L. L., Songaila A., Hu E. M., Cohen J. G., 1996, *AJ*, 112, 839  
 Cresci G., Davies R. I., Baker A. J., Lehnert M. D., 2005, *A&A*, 438, 757  
 Cresci G. et al., 2009, arXiv e-prints  
 Daddi E. et al., 2005, *ApJ*, 626, 680  
 Daddi E. et al., 2007, *ApJ*, 670, 156  
 Dalcanton J. J., 2007, *ApJ*, 658, 941  
 Davies R. I., 2007, *MNRAS*, 375, 1099  
 Dekel A., Birnboim Y., 2006, *MNRAS*, 368, 2  
 Dekel A., Sari R., Ceverino D., 2009, *ApJ*, in press (arXiv:0901.2458)  
 de Rossi M. E., Tissera P. B., Scannapieco C., 2007, *MNRAS*, 374, 323  
 Drory N., Alvarez M., 2008, *ApJ*, 680, 41  
 Dunne L. et al., 2009, *MNRAS*, 394, 3  
 Edmunds M. G., 1990, *MNRAS*, 246, 678  
 Eisenhauer F. et al., 2003, *Proc. SPIE*, 4841, 1548  
 Elbaz D. et al., 2007, *A&A*, 468, 33  
 Ellison S. L., Patton D. R., Simard L., McConnachie A. W., 2008, *ApJ*, 672, L107  
 Elmegreen B. G., 2002, *ApJ*, 577, 206  
 Erb D. K., 2008, *ApJ*, 674, 151  
 Erb D. K., Steidel C. C., Shapley A. E., Pettini M., Reddy N. A., Adelberger K. L., 2006a, *ApJ*, 644, 813  
 Erb D. K., Steidel C. C., Shapley A. E., Pettini M., Reddy N. A., Adelberger K. L., 2006b, *ApJ*, 646, 107  
 Erb D. K., Steidel C. C., Shapley A. E., Pettini M., Reddy N. A., Adelberger K. L., 2006c, *ApJ*, 647, 128  
 Fazio G. G. et al., 2004, *ApJS*, 154, 10  
 Förster Schreiber N. M. et al., 2006, *ApJ*, 645, 1062  
 Förster Schreiber N. M. et al., 2009, arXiv e-prints  
 Franx M. et al., 2003, *ApJ*, 587, L79  
 Franx M., van Dokkum P. G., Schreiber N. M. F., Wuyts S., Labbé I., Toft S., 2008, *ApJ*, 688, 770  
 Frye B., Broadhurst T., Benítez N., 2002, *ApJ*, 568, 558  
 Gallazzi A., Charlot S., Brinchmann J., White S. D. M., 2006, *MNRAS*, 370, 1106  
 Garnett D. R., 2002, *ApJ*, 581, 1019  
 Gavazzi G., Scodreggio M., 1996, *A&A*, 312, L29  
 Genzel R. et al., 2008, *ApJ*, 687, 59  
 Halliday C. et al., 2008, *A&A*, 479, 417  
 Hayashi M. et al., 2009, *ApJ*, 691, 140  
 Hopkins A. M., Beacom J. F., 2006, *ApJ*, 651, 142  
 Kannappan S. J., 2004, *ApJ*, 611, L89  
 Kennicutt J. R. C., 1998, *ARA&A*, 36, 189  
 Kennicutt J. R. C. et al., 2007, *ApJ*, 671, 333  
 Kewley L. J., Ellison S. L., 2008, *ApJ*, 681, 1183  
 Kobayashi C., Springel V., White S. D. M., 2007, *MNRAS*, 376, 1465  
 Kobulnicky H. A., Koo D. C., 2000, *ApJ*, 545, 712  
 Koopmans L. V. E., Treu T., 2003, preprint (astro-ph/0308056)  
 Köppen J., Weidner C., Kroupa P., 2007, *MNRAS*, 375, 673



- Lamareille F. et al., 2009, *A&A*, 495, 53
- Law D. R. et al., 2007, *ApJ*, 656, 1
- Lee H., Skillman E. D., Cannon M., Jackson D. C., Gehrz R. D., Polomski E. F., Woodward C. E., 2006, *ApJ*, 647, 970
- Lehnert M. D., Heckman T. M., 1996a, *ApJ*, 462, 651
- Lehnert M. D., Heckman T. M., 1996b, *ApJ*, 472, 546
- Lequeux J., Peimbert M., Rayo J. F., Serrano A., Torres-Peimbert S., 1979, *A&A*, 80, 155
- Liu X., Shapley A. E., Coil A. L., Brinchmann J., Ma C.-P., 2008, *ApJ*, 678, 758
- Maier C. et al., 2006, *ApJ*, 639, 858
- Maiolino R. et al., 2008, *A&A*, 488, 463
- Mannucci F., Pozzetti L., Thompson D., Oliua E., Baffa C., Comoretto G., Gennari S., Lisi F., 2002, *MNRAS*, 329, L57
- Mannucci F., Buttery H., Maiolino R., Marconi A., Pozzetti L., 2007, *A&A*, 461, 423
- Maraston C., 2005, *MNRAS*, 362, 799
- Marigo P., 2001, *A&A*, 370, 194
- Matteucci F., 2001, *The Chemical Evolution of the Galaxy*, *Astrophys. & Space Sci. Library*, Vol. 253. Kluwer, Dordrecht
- Matteucci F., 2008, in Grebel E., Moore B., eds, *Proc. 37th Saas-Fee Advanced Course, SSAA*, (arXiv:0804.1492)
- Michel-Dansac L., Lambas D. G., Alonso M. S., Tissera P., 2008, *MNRAS*, 386, L82
- Modigliani A. et al., 2007, *arXiv Astrophys. e-prints*
- Mori M., Umemura M., Ferrara A., 2004, *ApJ*, 613, L97
- Mouchine M., Gibson B. K., Renda A., Kawata D., 2008, *arXiv e-prints*
- Moustakas J., Kennicutt R. C., Jr., Tremonti C. A., 2006, *ApJ*, 642, 775
- Nagao T., Maiolino R., Marconi A., 2006, *A&A*, 459, 85
- Nesvadba N. P. H. et al., 2006, *ApJ*, 650, 661
- Nesvadba N. P. H. et al., 2007, *ApJ*, 657, 725
- Noeske K. G. et al., 2007, *ApJ*, 660, L47
- Panther B., Jimenez R., Heavens A. F., Charlot S., 2008, *MNRAS*, 391, 1117
- Pérez-González P. G., Gil de Paz A., Zamorano J., Gallego J., Alonso-Herrero A., Aragon-Salamanca A., 2003, *MNRAS*, 338, 525
- Perez-Montero E. et al., 2009, *A&A*, 495, 73
- Pettini M. et al., 2001, *ApJ*, 554, 981
- Pettini M., Rix S. A., Steidel C. C., Adelberger K. L., Hunt M. P., Shapley A. E., 2002, *ApJ*, 569, 742
- Pilyugin L. S., Vílchez J. M., Contini T., 2004, *A&A*, 425, 849
- Pozzetti L. et al., 2007, *A&A*, 474, 443
- Reddy N. A. et al., 2006, *ApJ*, 644, 792
- Rodrigues M. et al., 2008, *A&A*, 492, 371
- Saracco P. et al., 2003, *A&A*, 398, 127
- Saracco P. et al., 2005, *MNRAS*, 357, L40
- Savaglio S. et al., 2005, *ApJ*, 635, 260
- Scannapieco C., Tissera P. B., White S. D. M., Springel V., 2008, *MNRAS*, 389, 1137
- Schiminovich D. et al., 2007, *ApJS*, 173, 315
- Shapiro K. L. et al., 2008, *ApJ*, 682, 23
- Shapley A. E., Steidel C. C., Adelberger K. L., Dickinson M., Giavalisco M., Pettini M., 2001, *ApJ*, 562, 95
- Shapley A. E., Coil A. L., Ma C.-P., Bundy K., 2005, *ApJ*, 635, 1006
- Shen S. et al., 2003, *MNRAS*, 343, 978
- Somerville R. S., Hopkins P. F., Cox T. J., Robertson B. E., Hernquist L., 2008, *MNRAS*, 391, 481
- Stark D. P., Swinbank A. M., Ellis R. S., Dye S., Smail I. R., Richard J., 2008, *Nat*, 455, 775
- Steidel C. C. et al., 2003, *ApJ*, 592, 728
- Stewart K. R., Bullock J. S., Wechsler R. H., Maller A. H., Zentner A. R., 2008, *ApJ*, 683, 597
- Tacconi L. J. et al., 2006, *ApJ*, 640, 228
- Teplitz H. I. et al., 2000, *ApJ*, 533, L65
- Tornatore L., Borgani S., Dolag K., Matteucci F., 2007, *MNRAS*, 382, 1050
- Tremonti C. A. et al., 2004, *ApJ*, 613, 898
- Weiner B. J. et al., 2007, *ApJ*, 660, L39
- Weiner B. J. et al., 2008, *arXiv e-prints*
- Werner M. W. et al., 2004, *ApJS*, 154, 1
- Wolf C. et al., 2005, *ApJ*, 630, 771
- Woosley S. E., Weaver T. A., 1995, *ApJS*, 101, 181
- Zheng X. Z. et al., 2007, *ApJ*, 661, L41

This paper has been typeset from a  $\text{\LaTeX}$  file prepared by the author.